Marked highlighted manuscript

Alternative Lithium-Ion Battery Using Biomass-Derived Carbons as Environmentally Sustainable Anode

Celia Hernández-Rentero[1], Vittorio Marangon[2], Mara Olivares-Marín[3], Vicente Gómez-Serrano[3], Álvaro Caballero[1], Julián Morales[1]* and Jusef Hassoun[2]*

[1] Department of Química Inorgánica e Ingeniería Química, Instituto de Química Fina y Nanoquímica, University of Córdoba, 14071 Córdoba, Spain

[2] Department of Chemical and Pharmaceutical Sciences, University of Ferrara, Via Fossato di Mortara 17, Ferrara 44121, Italy

[3] Department of Química Inorgánica, Facultad de Ciencias, University of Extremadura, 06006 Badajoz, Spain

*Corresponding Authors. Tel: +39 0532-455163, E-mail: jusef.hassoun@uniroma1.it (Jusef Hassoun), Tel: +34 957218620, E-mail: iq1mopaj@uco.es (Julián Morales)

Abstract

Disordered carbons derived from biomass are herein efficiently used as an alternative anode in lithium-ion battery. Carbon precursor obtained from cherry pit is activated by using either KOH or H_3PO_4, to increase the specific surface area and enable porosity. Structure, morphology and chemical characteristics of the activated carbons are investigated by X-ray diffraction (XRD), transmission electron microscopy (TEM), scanning electron microscopy (SEM), thermogravimetry (TG), Raman spectroscopy, nitrogen and mercury porosimetry. The electrodes are studied in lithium half-cell by galvanostatic cycling, cyclic voltammetry, and electrochemical impedance spectroscopy (EIS). The study evidences substantial effect of chemical activation on the carbon morphology, electrode resistance, and electrochemical performance. The materials reveal the typical profile of disordered carbon with initial irreversibility vanishing during cycles. Carbons

activated by H_3PO_4 show higher capacity at the lower c-rates, while those activated by KOH reveal improved reversible capacity at the high currents, with efficiency approaching 100% upon initial cycles, and reversible capacity exceeding 175 mAh g^{-1}. Therefore, the carbons and $LiFePO_4$ cathode are combined in lithium-ion cells delivering 160 mAh g^{-1} at 2.8 V, with a retention exceeding 95% upon 200 cycles at C/3 rate. Hence, the carbons are suggested as environmentally sustainable anode for Li-ion battery.

1. Introduction

Lithium-ion battery is the most diffused energy storage system for modern applications such as computers, electronic devices, and electric vehicles (EVs) [1]. This important system may actually satisfy the increasing demand for energy storage from renewable sources for mitigating climate change issues, which are possibly driven from the use of fossil fuels, and related greenhouse gasses emission [2,3]. Lithium-ion battery, in its most conventional configuration, is formed by electrodes based on Li^+ intercalation or insertion materials at the cathode, such as $LiCoO_2$ and $LiFePO_4$, and graphite at the anode side, separated by an inorganic electrolyte dissolving a lithium salt (e.g., EC:DMC, $LiPF_6$) [1,4]. Since first commercialization by Sony Corporation during 1991[5] LIB employs graphite as the preferred anode, with a theoretical specific capacity of 372 mAh g^{-1} [6], while only few other examples of practical interest, such as Si and Sn-based materials [7,8], carbon/alloy mixtures [9,10], and lithium titanate spinel oxide [11] have been proposed as alternative materials. A great number of studies has focused on various carbonaceous materials alternative to graphite for application as anodes in LIBs [12–18]. Suitable characteristics for enabling the energy storage properties of carbons are an increased active surface area for ensuring sufficient contact between electrode and electrolyte, the presence of pores, and their size distribution. The latter characteristic plays a key role for enhancing the electrochemical process since micro-pores can fasten ions exchange, whereas the meso- and macro-pores act as a reservoir for active ions [19]. Furthermore, an increased awareness for environmental issues driven from CO_2

emission by biomass burning promoted several efforts for entrapping C in sustainable materials [20]. Therefore, biomass-derived carbon electrodes have attracted relevant attention due their structural versatility, tunable physical/chemical properties, environmental friendliness, and considerable economic value [21]. These substrates were actually employed in various energy-storage systems such as Li-ion, Na-ion and supercapacitors. Indeed, a recent paper reported ultrafine CoP nanoparticles embedded in carbon nanorod grown on the biomass-derived carbon (BC), that is, CoP@C/BC, as anode materials for lithium-ion batteries with a specific capacity of about 300 mAh g^{-1}, and an outstanding long-term cycling performance of about 1000 cycles [22]. Another effective method employed buckwheat hulls as the precursor to prepare oxygen-doped hard carbon by simple carbonization [23]. The electrode reveled in sodium battery a maximum reversible capacity of 400 mA h g^{-1} at 50 mA g^{-1}, and capacity retention of 96% with respect to the initial capacity (about 110 mAh g^{-1}) over 3000 cycles at 2A g^{-1}. Furthermore, all carbon-based Li-ion capacitor was obtained from environmentally threatening prosopis juliflora [24]. The pyrolyzed carbon exhibited a few layers of graphene-like structure, and tubular morphology with multiple inherent heteroatoms like N, S, and Ca which enhanced electrical conductivity, pore generation, thus improving capacity/capacitance of carbonaceous materials. The material has been lithiated, and it delivered an energy density of about 216 Wh kg^{-1}, retaining about 94% initial capacity after 5000 cycles [24]. Various carbons, obtained from loofah [25], coffee [26], honey [27], walnut shells [28], and cherry pits [29] residues, have been already reported as suitable electrode for lithium-ion battery, while other activated carbons derived from bamboo [30], natural seed [31], corncobs [32] or tea [33] residues have also been proposed for sodium batteries. In addition, olive stone [34], almond shell [35], walnut shell, peanut shell, and pistachio hull [36], have been used as precursor for carbons employed in Li-S batteries.

Herein, we propose an alternative carbon electrode obtained from the ligno-cellulosic waste of cherry pits (CP), which is considered a viable raw material since produced by a relevant amount (e.g., with global production of cherry in 2017 of about 2.5 millions of tons mainly used for Kirsch,

beers, jams, chocolates, manufacturing [37]). Generally, carbonaceous substrates obtained from bio-residues require an activation procedure involving chemical agents, such as bases (e.g., KOH) or acids (e.g., H_3PO_4), and thermal steps (e.g., annealing under Ar, Ar/H_2 or N_2 atmosphere), for removing organic fractions and promoting carbon porosity and surface characteristics suitable for application in battery [27,28,32,38,39]. In particular, potassium hydroxide (KOH) favors chemical activation according to a complex mechanism involving the formation of K_2CO_3, K_2O, and possibly reducing species such as metallic K, while thermal treatment generally produce water vapor, CO_2, and CO gasses leading to a physical activation [40]. Furthermore, phosphoric acid (H_3PO_4) can generate P-containing functional groups into the carbon matrix [41], which may promote the formation of micro-pores into the carbon, and actually improve the electrochemical stability of the material in battery [42]. We have previously shown the possible application of a carbon derived from cherry pits biomass activated by H_3PO_4 as a substrate in lithium-sulfur battery [43]. In this work, we extend our study by reporting carbons obtained from cherry pits, activated both by H_3PO_4 and KOH, and differing by the porosity nature and degree, for application in an alternative Li-ion battery using the $LiFePO_4$ cathode. $LiFePO_4$ is an olivine-structure materials characterized by a flat plateau at 3.5 V, a theoretical specific capacity of 170 mAh g^{-1}, and a relevant stability in lithium cell [44,45]. The carbon materials are fully characterized in terms of structure, morphology, and electrochemical behavior, and efficiently used in full cells characterized by an extended cycle life and a remarkable environmental compatibility.

2. Experimental section

2.1 *Synthesis of the active materials*

The two samples studied in this work were derived from biomass residues of cherry pits (CP), supplied by Asociación de Cooperativas del Valle del Jerte (Cáceres province, Spain). After being dried, and ground, the biomass residues of cherry pits (i.e., a sample still not suitable for battery testing due to the organic residue) were sized and the fraction of particle between 1 and 2 mm was

chosen. 50 g of residues were immersed in 250 mL of diluted H_2SO_4 solution (5 vol.%) for 24 h, filtered, and washed with distilled water until pH reached a value of 6 in the residual liquid. The resulting powder (CP) was processed according to previous reports, as summarized in Table 1. Accordingly, two different activation agents (AA), that is, potassium hydroxide (KOH) [46] (sample AC-K) and phosphoric acid (H_3PO_4) [47] (sample AC-H) were used. 25 g of powder were dispersed in distilled water, and added by the specific amount (Table 1) of either H_3PO_4 (85wt.% in H_2O, 99.99%, Sigma Aldrich) or KOH (ACS reagent, ≥85%, pellets, Sigma Aldrich). Subsequently, the samples were dried for 24 h at 100 °C, annealed for 2 h at 800 °C under N_2 atmosphere with a flow of 100 mL/min and heating rate of 10 °C/min, washed with diluted HCl, with distilled water until a pH value above 6, and finally dried in oven at 120 °C overnight.

The $LiFePO_4$ material was described a previous paper [48].

Table 1. Synthesis conditions of the activated carbons reported in this work

Sample acronym	Activation Agent (AA)	Preparation			
		CP (g)	AA (g)	T_C (°C)	t (h)
AC-H	H_3PO_4	25	44	800	2
AC-K	KOH	25	25	800	2

2.2 *Materials characterization*

The elemental chemical analysis of activated carbons was carried out using a LECO CHNS-932 micro-analyser coupled with a VTF900 furnace for oxygen. The system enables the analysis of carbon, hydrogen, nitrogen, and sulfur separately from oxygen. The structural properties were examined using XRD, Raman and FT-IR spectroscopy. The XRD patterns were obtained with a Bruker D8 Discover X-ray diffractometer, using CuKα radiation, and a Ge monochromator within a range of 2-80˚ (2θ) using a step size of 0.04° and 1.05 s per step. Raman measurements were performed under ambient conditions through a Renishaw inVia Microscope equipped with a Renishaw CCD Camera (578 x 400) detector, and a 532 nm edge in line focus mode laser. The FT-

IR spectra were recorded in a Perkin-Elmer 1720 FT-IR spectrometer in the 4000–400 cm^{-1} wavenumber range, 40 scans being taken at 2 cm^{-1} resolution. Pellets were prepared by mixing powdered sample, and KBr (Merck, for spectroscopy) at a sample/KBr weight ratio of 1:500. Each mixture was compacted at 10 tonnes cm^{-1} for 3 min, using a Perkin-Elmer hydraulic press.

The textural properties were examined by nitrogen, and mercury porosimetry. Autosorb-1 semiautomatic apparatus (Quantachrome) using nitrogen as an adsorbent was used to obtain the micropore volume (V_{mi}), by applying the Dubinin–Radushkevich equation [49]. The pore size distribution of the carbons in the micropore and narrow mesopore ranges was obtained by applying the density functional theory (DFT) method. Macropore, and mesopore volumes were determined by a mercury porosimeter Autoscan-60 (Quantachrome). From the plots of cumulative pore volume (V_{cu}) versus pore radius (r), macropore volume, $V_{ma} = V_{cu}$ (at r = 250 Å), and mesopore volume, $V_{me} = V_{cu}$ (at r < 20 Å) – V_{ma}, of the samples were obtained. Finally, the total pore volume (V_T) was estimated by using of the equation $V_T = V_{mi} + V_{me} + V_{ma}$.

Thermogravimetric analysis (TGA) was performed by using a Mettler Toledo TGA/DSC-1 at a heating rate of 10 °C min^{-1} from 30 to 800 °C, under an oxygen atmosphere. Before the measurements, the samples were dried overnight at 120ºC to remove traces of moisture.

Sample's morphology was studied by transmission electron microscopy (TEM), using a Zeiss EM 910 microscope equipped with a tungsten thermoionic electron gun operating at 100 kV, and scanning electron microscopy (SEM), using a Zeiss EVO 40 microscope equipped with a LaB_6 thermoionic electron gun. Energy-dispersive X-ray spectroscopy (EDS) was recorded on the SEM images through a X-ACT Cambridge Instruments analyzer to study the element distribution.

2.3 *Electrode preparation and electrochemical characterization*

The electrodes were prepared by mixing the active material, either carbons or $LiFePO_4$, with carbon super P (Timcal, conducting agent) and polyvinylidene fluoride (PVDF 6020, Solef Solvay, binder) in a weight proportion of 80:10:10, and adding 1-methyl-2-pyrrolidinone (NMP, Sigma-Aldrich) to

obtain a slurry for coating the electrode material on a Cu foil (MTI, 18µm) (carbons) or Al foil ($LiFePO_4$), using Doctor-Blade technique. The slurry was heated for 3 h at 70˚C by using a hot plate to remove the solvent, and finally cut into disks (either 10 or 14mm diameter), which were dried at 105˚C overnight under vacuum. The loading of the active material in the final electrode was about 3,5 mg cm^{-2} for carbons and 4 mg cm^{-2} for $LiFePO_4$.

The electrochemical process of the carbon materials was evaluated both in 2032 coin-type cells and 3-electrode T-cell, prepared in an Ar-filled glove box (MBraun, O_2 and H_2O content below 1 ppm), with a Li/ EC, DMC 1:1 (w/w), 1 M $LiPF_6$/carbon configuration, using the selected carbon as the working electrode (14 mm-diameter in coin cell and 10 mm-diameter in T-cell), a Whatman disk soaked with the electrolyte as the separator, and a lithium metal disk as the counter and reference electrode.

Cyclic voltammetry (CV) and Electrochemical impedance spectroscopy (EIS) tests were performed by using 3-electrode T-cell through a VersaSTAT MC Princeton Applied Research (PAR) analyzer. CV measurements consisted of ten cycles in the 0.01–2.8 V range with a scan rate of 0.1 mV s^{-1}, while EIS measurements were taken at the open circuit (OCV), after the first, fifth, and tenth CV cycle in the 500 kHz–100 mHz frequency range using a 10 mV signal amplitude.

Galvanostatic cycling tests were performed in coin-type cells by using a MACCOR series 4000 battery test system within the potential window 0.01–2.8 V. Rate Capability measurement was performed using current values of C/10, C/5, C/3, C/2, 1C, 2C and 5C (1C = 372 mAg^{-1}). Galvanostatic tests prolonged to 200 cycles were performed at constant rate of C/3. Both specific current and specific capacity were referred to the carbon mass, that is, the electrochemically active component in the electrode.

The stability of the two carbon materials in lithium cell upon prolonged galvanostatic cycling at C/3 (1C = 372 mA g^{-1}) was evaluated by performing EIS measurements at the OCV, and after the first,

tenth, and hundredth discharge/charge cycle in the 500 kHz–100 mHz frequency range using a 10 mV signal amplitude.

The performance of the $LiFePO_4$ cathode in lithium cell was investigated by a galvanostatic cycling test using a constant current rate of C/3 (1C = 170 mA g^{-1}) for over 100 cycles in the 2.7–4.0 V range. The cell was assembled by adopting the Li / EC, DMC 1:1 (w/w), 1 M $LiPF_6$ / $LiFePO_4$ configuration, using a Celgard separator soaked with the electrolyte. Both specific current and specific capacity were referred to the $LiFePO_4$ mass.

The lithium-ion full cells were assembled by coupling the selected carbon (either AC-K or AC-H) with a $LiFePO_4$ cathode in 2032 coin-type cells using the configuration Carbon/EC, DMC 1:1 (w/w), 1 M $LiPF_6$ /$LiFePO_4$. Before use in Li-ion cell, the carbon electrodes were pre-activated by 30 galvanostatic cycles in lithium half-cell at a current rate of C/3 (1C = 372 mA g^{-1}) in a coin cell with the above mentioned configuration. After activated, the carbon electrodes were washed using DMC, dried under vacuum for 30 min, and employed in the above described Li-ion cell as the negative electrode.

Cycling tests of the Li-ion cells were performed using a MACCOR series 4000 battery test system within the potential window 0.2–3.8 V. Rate capability measurements were performed using current values of C/5, C/3, 1C and 2C (1 C = 170 mA g^{-1}). Galvanostatic tests prolonged over 200 cycles were performed at a current rate of C/3. Both specific current and specific capacity of the full-cell were referred to the $LiFePO_4$.

3. Result and discussion

Coals composition is detected by elemental analysis and reported in terms of weight % in Table 2. The carbon activated with KOH reveals higher content of C (about 89%), less O (about 8%) and H (about 1%), compared to the sample activated by H_3PO_4 (about 81%, 11% and 2%, respectively), while N and S contents appear almost negligible for both samples (i.e., lower than 1%). Relevantly,

AC-K evidences an overall element content higher than 99%, instead AC-H shows an elemental content of about 94%, thus suggesting the additional presence of different atoms in the latter carbon. X-ray energy dispersive spectroscopy (EDS) of the AC-H sample reported subsequently (see Fig. 3) indicates phosphorous (P) as that the additional element (around 6% weight) by.

Table 2. Elemental analysis of AC-K and AC-H samples: weight % of C, H, N, S and O, respectively.

Sample	C	H	N	S	O	Sum
AC-K	88.99	1.05	0.65	0.05	8.34	99.08
AC-H	80.57	2.0	0.18	0.06	11.40	94.21

The structural characteristics of the carbon samples investigated in this work are summarized in Figure 1. Indeed, Fig. 1a shows the XRD patterns of AC-K (red line) and AC-H (green line) as well as the reference patterns of graphite (PDF # 41-1487). The figure evidences for both samples similar patterns characterized by the absence of defined peaks of ordered graphite, while the presence of two weak and broad signals around $2\theta = 26^{o}$ and 44^{o}, which can be likely attributed to the (0 0 2) and (1 0 0) reflections of highly disordered carbons [50,51]. Furthermore, the Raman spectra of Fig. 1b show the D and G bands of carbon at approximately $\tilde{\nu}$=1346 and 1594 cm^{-1}, respectively, with an intensity ratio (I_D/I_G) of 0.96 in AC-K and 0.95 in AC-H. The relatively high I_D/I_G value likely indicates a pronounced defect content and a small average size of the sp^2 domains [52]. It is worth mentioning that the slightly lower intensity of the XRD reflections and higher I_D/I_G value of the AC-K sample may likely suggest a more effective activation the carbon sample by using KOH rather than H_3PO_4 [42,43,46,47]. Relevantly, the TGA curves performed under oxygen and reported in Fig. 1c reveal a different trend for the two studied carbons. The two samples begin losing weight from about 200 °C, most likely due to organic residues which are more relevant in AC-K (about 18 % of weight loss until 450 °C) compared to AC-H (about 7% weight loss until 450

°C). Both samples reveal a fast decay of the weight around 500 °C due to the full oxidation of the carbon to CO_2. However, this pronounced weight loss represents more than 95% in the sample activated with KOH and only 40% when the activation is carried out with H_3PO_4. Therefore, the weight loss of the AC-H sample at temperatures higher than 500 °C may be likely ascribed to acid impurities rather than the exclusive pyrolysis of C. The inset of Fig. 1c, reporting the DTG curves, evidences at least two stages of weight loss for AC-H (green curve), that is, just above 500 °C and at about 650 °C, while only the main peak around 500 °C for AC-K (red curve). Lignocellulosic materials react with H_3PO_4 according to a complex bond-breaking process involving CO, CO_2 and CH_4 gases evolution, even at low temperatures, with formation of phosphate esters by cellulose phosphorylation [53]. On the other hand, appreciable presence of P is actually suggested by EDS hereafter, while the presence of phosphorylated functional groups is confirmed by the FT-IR spectra of the AC-H sample reported in Fig. 1d. The latter figure shows the absorption spectra of carbon samples activated using H_3PO_4 by heating at various temperatures between 350 and 550 ºC, that is, temperature range corresponding to the change of TG curve's slope observed in Fig. 1c. The FT-IR spectra reveal a series of shoulders and absorption bands whose position and allocation are detailed in Table 3 [54].

Table 3. Assignment of absorption bands of the FT-IR spectra of AC-H sample (cm^{-1}) collected in Fig. 1d.

Wavenumber / cm^{-1}	Assignments	Group
3388	ν (O−H)	Intermolecular hydrogen bond: alcohols, phenols and carboxylic acids
1693	ν (C=O)	Esters: quinone and carboxylic acids
1577	ν (C=C)	Olefinic groups and aromatic rings
1175	ν (C−OH)	Phenols and carboxylic acids
	ν (C−O) in C−O−C	Ethers

	ν (P=O)	Phosphate esters and polyphosphate
1001	ν (P−OH)	Phosphate esters and polyphosphate
	ν (C−O) in P-O-C	Phosphate esters and polyphosphate
912	ν (P−O) in P-O-C	Phosphate esters and polyphosphate

As above mentioned, elemental analysis (see Table 2) and EDS suggest for the carbons surface groups involving both O and P, despite the repeated washing adopted to leach the phosphorus species. Interestingly, the relative intensity of the IR bands located between 1600 and 1200 cm^{-1} (Fig. 1d) tends to increase by raising the temperature from 350 and 500 °C, thus suggesting increased concentration of surface groups with C= C, C─O and/ or P = O bonds, while a further temperature raise leads to the decrease of the functional groups content. Therefore, the weight loss at temperature higher than 500 °C observed by thermogravimetry (Fig. 1c) would mainly correspond to the gasification of carbon, while at higher temperatures additional phases related to the phosphorous groups would also be volatilized, thus accounting for the AC-H thermogram complexity observed in Fig. 1c.

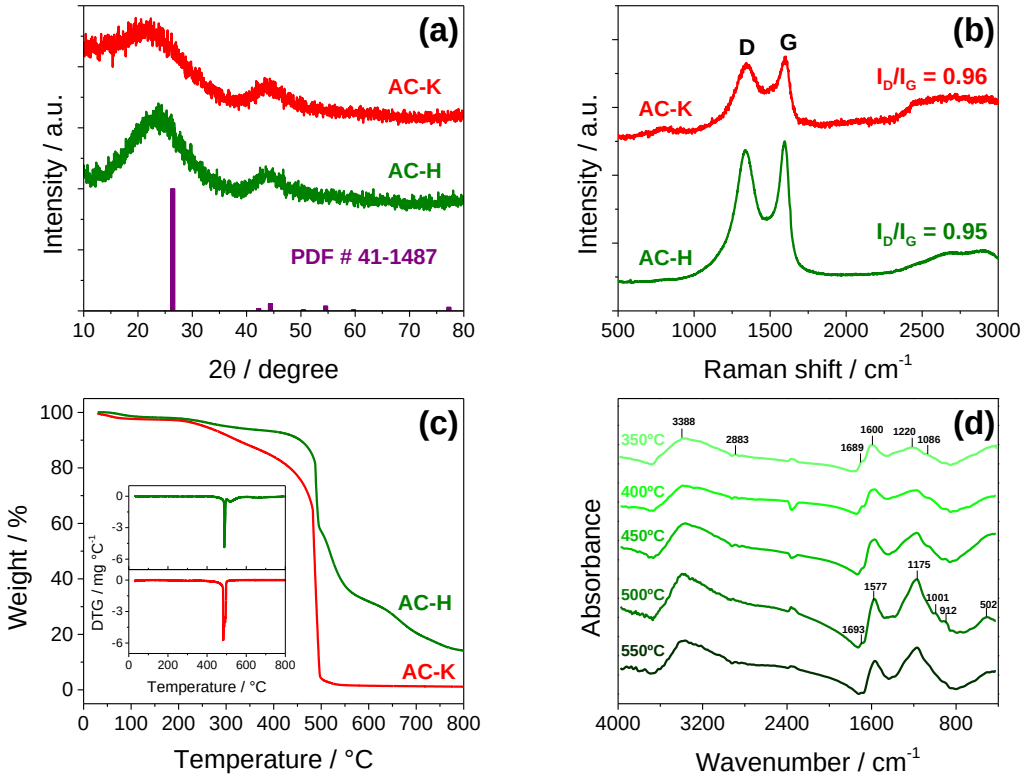

Figure 1. **(a-c)** Structural study of the samples**.** (**a**) X-ray diffraction patterns (XRD), (**b**) Raman spectra, (**c**) Thermogravimetric Analysis (TGA) under oxygen atmosphere of AC-K (red line) and AC-H (green line); (insert: DTG curves) **(d)** FT-IR spectra of the AC-H sample heated at different temperatures. See experimental section for sample's acronym.

The high ash content in AC-H, around 15%, is also observed in other biomass-derived carbons activated with H_3PO_4 [55] in a much higher ratio than samples activated by KOH such as AC-K. Therefore, the thermal measurements reveal substantial differences between the two sample, and likely suggest a more relevant organic fraction for AC-K while a more significant inorganic residue for AC-H.

The effects of the activation conditions on the surface area and the pore volume of the two samples are evaluated by N_2 and Hg adsorption-desorption measurements reported in Figure 2 and summarized in Table 4. The N_2 adsorption isotherms of the two activated carbons shown in Fig. 2a reveal the expected trends, both belonging to a type I BDDT classification, typical of microporous solids with relatively small external surfaces. The higher adsorption values of the sample AC-H with respect to AC-K observed in Fig. 2a indicate extended surface area of the former compared to the latter, that is, 1662 and 1171 $m^2\ g^{-1}$, respectively, possibly suggesting a more efficient removal of the organic part by means of H_3PO_4 rather than KOH, in line with the TG measurements [46,47]. Although the two samples have the same micro-pore volume (V_{mi}), approaching 0.6 $cm^3\ g^{-1}$, and an overall-pore volume (V_T) only slightly higher for AC-K compared to AC-H, with values of about 1.1 and 1.0 $cm^3\ g^{-1}$, respectively, the DFT plots of Fig. 2b show appreciable differences in pore size. Indeed, AC-K has pores with an average size below 0.8 nm, instead AC-H pores range around 1.5 nm. The analysis of the Hg porosimetry data reported in Fig. 2c shows relevantly different distribution of macro- and meso-pores (see table 4). AC-H has meso-pores with a volume (V_{me}) of about 0.4 $cm^3\ g^{-1}$, and a much lower macro-pores volume (i.e., V_{ma} of about 0.08 $cm^3\ g^{-1}$) compared to AC-K which contains predominantly macro-pores (V_{ma} = 0.5 $cm^3\ g^{-1}$). Furthermore, AC-K shows a slightly higher overall porosity compared to AC-H, that is, 1.13 and 0.97 $cm^3\ g^{-1}$,

respectively (V_T in Table 4). These remarkable differences indicate an actual effect of the activation conditions on the samples characteristics, and suggest a careful selection of the operating conditions adopted during the synthesis for achieving the appropriate properties.

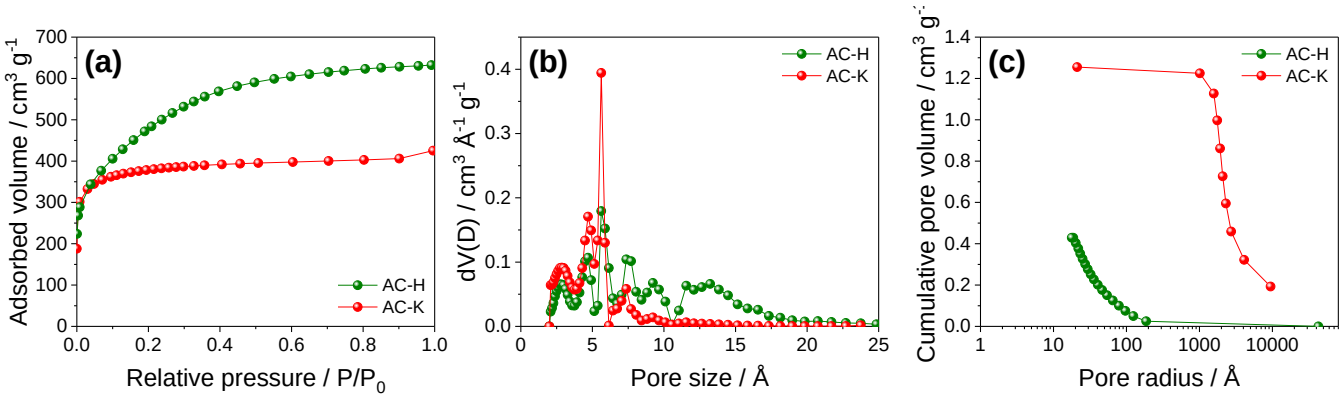

Figure 2. (a) N_2 adsorption BET isotherms recorded at 77 K, **(b)** pore size distribution obtained by density functional theory (DFT), and **(c)** cumulative pore volume trending determined by Hg porosimetry of AC-K (red) and AC-H (green) samples. See experimental section for sample's acronym.

Table 4. Surface area (S_{BET}), and micro-pores volume (V_{mi}) of AC-K, and AC-H as determined by N_2 adsorption-desorption BET isotherms. Volume of meso-pores (V_{me}), and macro-pores (V_{ma}) of AC-K, and AC-H as determined by Hg-porosimetry. V_T represents the overall sample porosity. See experimental section for sample's acronym.

Sample	S_{BET} ($m^2\ g^{-1}$)	V_{mi} (N_2) ($cm^3\ g^{-1}$)	V_{me} (Hg) ($cm^3\ g^{-1}$)	V_{ma} (Hg) ($cm^3\ g^{-1}$)	V_T (Hg) ($cm^3\ g^{-1}$)
AC-K	1171	0.57	0.08	0.48	1.13
AC-H	1662	0.57	0.40	0.08	0.97

Several literature papers have indicated the role of combination of the macro-, meso- and micro pores in enhancing the electrode performances in terms of *i)* electrolyte accessibility, and electrode wettability, which are particularly promoted by the macro and meso-pores [19], *ii)* ion diffusion

rate, and iii) charge transport kinetics at the electrode/electrolyte interphase which is mainly ascribed to micro pores [56]. Accordingly, a promoted electrolyte accessibility limits the cell polarization, thus favoring the energy efficiency, while low charge-transfer resistance, and fast ion diffusion at the electrode/electrolyte interphase favor the rate capability of the porous carbon materials [57]. Therefore, the simultaneous presence of various types of porosity into the hierarchical carbon actually allows enhanced performances of the electrode in energy storage devices [56].

The morphological characteristics of the samples are delighted by SEM, and TEM as reported in Figure 3. The samples reveal primary micrometric particles with bigger size for AC-K (about 200 μm, SEM in Fig. 3b) compared to AC-H (about 60 μm, Fig. 3d), likely due to the different activation pathway, as well as secondary particles with a size of about 20 μm (SEM insets in Fig. 3b and Fig. 3d). Flakes having submicron dimensions are also observed by the TEM images (Fig. 3a, c), mostly due to exfoliation of the carbon during the synthesis. Furthermore, the uniform presence of P into the AC-H sample, not detected by elemental analysis in Table 2, is herein confirmed by EDS mapping as reported in inset of Fig. 3d.

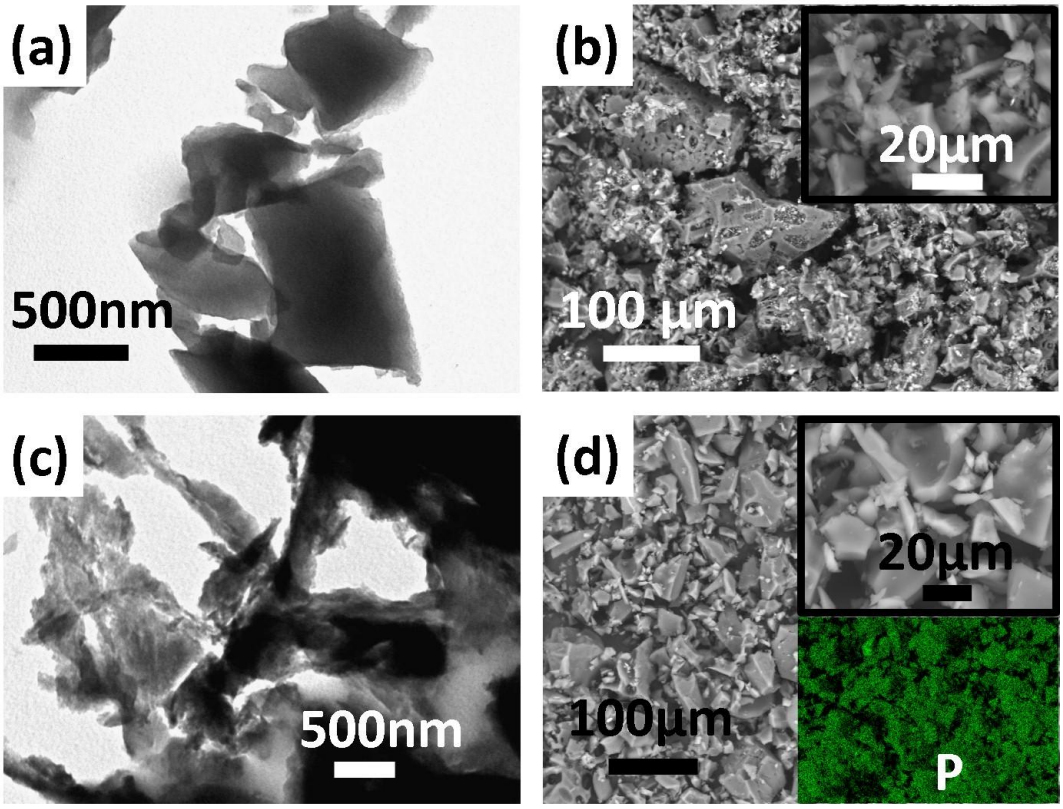

Figure 3. (**a**-**d**) Morphological study of the samples. (**a**, **c**) Transmission Electron Micrographs (TEM), (**b**, **d**) Scanning Electron Micrographs (SEM) of AC-K and AC-H, respectively. EDS mapping of P in AC-H sample is shown in the inset of Fig. 3d. See experimental section for sample's acronym.

The carbon electrodes are subsequently studied in lithium cell by combining voltammetry, impedance spectroscopy and galvanostatic measurements. Fig. 4a, and Fig. 4c show respectively the CV scans of AC-K, and AC-H electrodes in a three-electrode lithium cell between 0.01 and 2.8 V at a rate of 0.1 mV s^{-1}. Both samples show during the first cathodic scan a voltammetry profile significantly differing from the subsequent, characterized by a substantial irreversibility. Indeed, AC-K evidences only a broad signal extending below 1.0 V vs. Li^+/Li (inset of Fig. 4a), while the AC-H shows a first reduction peak at about 1.2 V, a small signal at about 0.7 V followed by a tilted line extending to 0.01 vs. Li^+/Li (inset of Fig. 4c). The differences between the curves related to AC-H and AC-K is particularly evidenced by the presence during the first cathodic scan of a peak at

the higher voltage value, i.e., 1.2 V vs. Li^+/Li, in the former and its absence in the latter. This discrepancy may be likely ascribed to the different nature, and extent of the impurities in the two electrodes. The elemental analysis of Table 2 actually reveals that AC-H contains about 6% of additional impurity compared to AC-K, which has been detected as P in the inset of the revised version of Fig. 3d. This impurity may possibly justify the side irreversible peak in the voltammetry curve related to AC-H. The irreversible trend of the first reduction is a typical characteristic of the electrochemical process in the carbons due to partial decomposition of the electrolyte, and the formation of a solid electrolyte interphase (SEI) layer at the electrode/electrolyte interphase [58,59]. The CV data also suggest additional irreversible processes ascribed to the specific impurities in the two carbon (revealed by TG and EDS): hence, AC-K mostly has organic residues while AC-H contains mainly an inorganic fraction constituted by phosphates [30]. The subsequent CV cycles are characterized by reversible, progressively overlapping profiles, with broad signals around 1.0 V, 0.2 V and 0.01 V vs. Li^+/Li due to the insertion/de-insertion of the lithium into the disordered carbon as well as to possible lithium plating/stripping into the pores of the active materials [60]. The achieved reversibility upon the first CV cycles likely indicates the stability of the SEI formed by the above mentioned irreversible reduction of the electrolyte [58–60], and of the residues detected in the activated carbons [38,61]. Additional insight on the electrode/electrolyte interphase characteristics are given by EIS analyses at the open-circuit voltage (OCV) and upon CV of the lithium cells using AC-K (Fig. 4b), and AC-H (Fig. 4d). Beside the electrolyte resistance, represented by the high-frequency intercept, the Nyquist plots show a middle-high frequency semicircle or deeply convoluted semicircles, accounting for both charge transfer and SEI film contributions in the electrode/electrolyte interphase, and a low-frequency tilted line with a slope approaching 45° likely related to the Warburg-type semi-infinite diffusion in the electrode or to cell geometric capacity [62–64]. Table 5 reports the values of the electrode/electrolyte interphase resistance, and the chi-square (χ^2) values obtained by nonlinear least squares (NLLS) method using a Boukamp tool [65], by adopting the equivalent circuits $R_e(R_iQ_i)Q_g$, where (R_iQ_i) are the resistances and the constant-

phase elements of the middle-high frequency semicircles ascribed to the interphase, R_e the electrolyte resistance, and Q_g the constant phase element related to the low-frequency line [66]. The accuracy of the data obtained by the analysis, evidenced by χ^2 values of about 10^{-4} or below, is achieved by adopting either one or two RQ elements, that is, $R_e(R_1Q_1)Q_g$ or $R_e(R_1Q_1)(R_2Q_2)Q_g$ for the analysis of the middle-high frequency semicircle of the interphase for AC-K, and AC-H electrodes, respectively. This discrepancy may be partially justified by a SEI film, and charge transfer processes having significantly different time-constant in AC-K and AC-H electrode/electrolyte interphase, leading to elements overlapping in one only in the latter, and to two distinguishable elements in the former [65,67]. Interestingly, Table 5 evidences that the first element vanishes by the ongoing of the voltammetry of the Li-cell using AC-K, with resistance value decreasing from about 7 Ω at the OCV to 1 Ω after 10 CV cycles.

Further difference between AC-K and AC-H interphases can be observed by taking into account the overall interphase resistance (R) reported in Table 5, and plotted in the inset of the corresponding Nyquist plot of Fig. 4b, and Fig. 4d, respectively. The figure reveals higher resistance for AC-K compared to AC-H with values of about 33 Ω and 3 Ω, respectively, at the OCV. After 1 CV cycle, the resistance decreases to about 21 Ω for AC-K, while it raises to about 24 Ω for AC-H, to finally increase after 5 and 10 CV cycles to 43 Ω, and 78 Ω for AC-K, and to 32 Ω, and 40 Ω for AC-H, respectively. These trends as well as the different CV responses may be likely ascribed to the nature of each carbon in terms of composition, and morphology which may actually influence the electrochemical behavior of the electrode, and of possible side reaction [68,69].

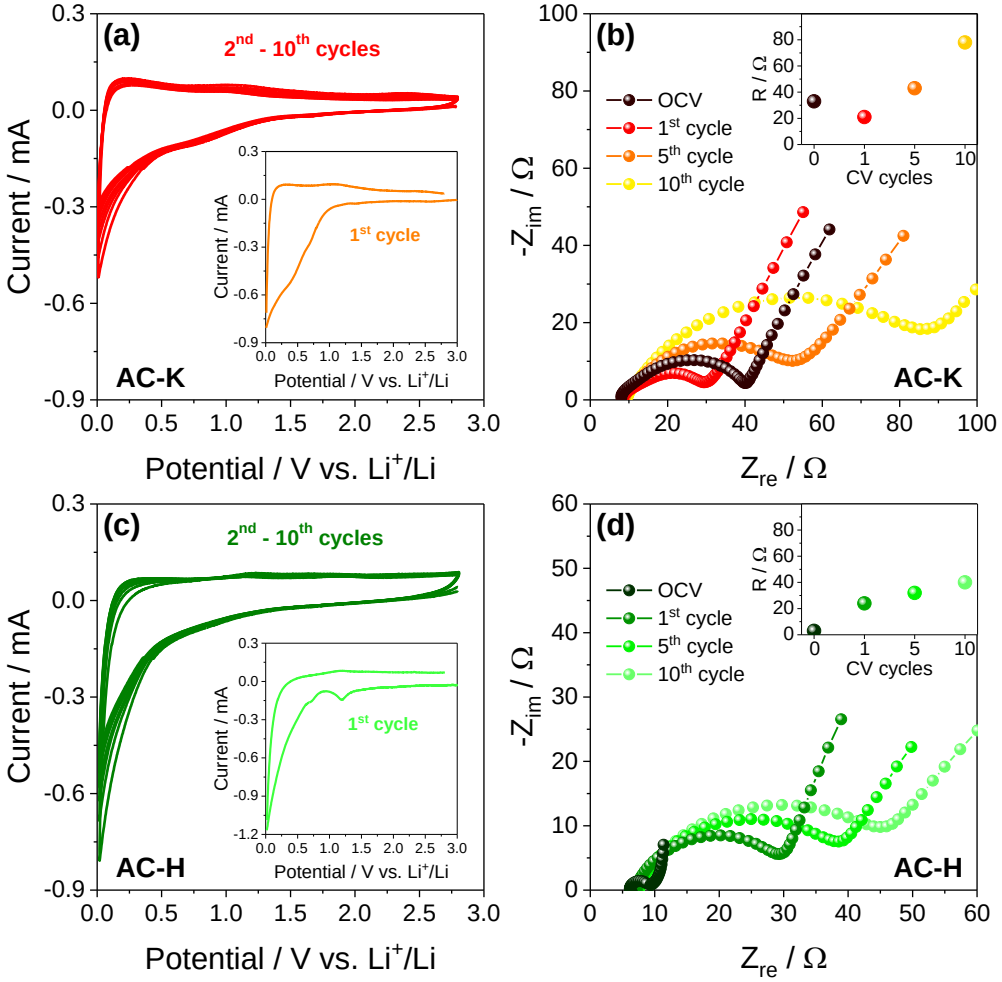

Figure 4. (**a-d**) Electrochemical features of the electrodes and characteristics of the electrode/electrolyte interphase. (**a**, **c**) Cyclic voltammetry profiles (CV) of (**a**) AC-K and (**c**) AC-H in three-electrode T-cell using lithium as counter and reference electrodes at a scan rate of 0.1 mV s^{-1}, from 0.01V to 2.8V, and (**b**, **d**) corresponding Nyquist plot of the Electrochemical Impedance Spectroscopy (EIS), respectively, at the OCV, after 1, 5 and 10 voltammetry cycles. Electrolyte: EC, DMC 1:1 (w/w), 1M $LiPF_6$. Alternate signal amplitude: 10 mV. Frequency range: 500 kHz - 100 mHz. Temperature: 25 °C. See experimental section for sample's acronym.

In this respect, it may be worth noting that the additional decomposition peak at about 1.2 V vs. Li/Li^+ observed for AC-H during the first cathodic scan (inset of Fig 4c) may actually lead to the initial increase of the interphase resistance observed in inset of Fig. 4d, while CV profile in AC-K (inset of Fig. 4a) can likely favor the SEI formation as suggested by the initial impedance decrease

in the corresponding trend in inset Fig. 4b. On the other hand, the subsequent CV cycles lead for both samples to an increase of the interphase resistance due to the SEI growth.

Table 5. Electrode/electrolyte interphase resistance and chi-square (χ^2) values obtained by NLLS analyses using a Boukamp tool of the impedance spectra of AC-K (Figure 3b), and AC-H (Figure 3d) in three-electrode T-cell using lithium as counter and reference electrodes at the OCV, after 1, 5 and 10 voltammetry cycles at a 0.1 mV s^{-1} scan rate within the potential range from 0.01 to 2.8 V vs Li^+/Li (reported in Figure 3a and Figure 3b, respectively). Electrolyte: EC, DMC 1:1 (w/w), 1M $LiPF_6$. Alternate signal amplitude: 10 mV. Frequency range: 500 kHz - 100 mHz. Temperature: 25 °C. See experimental section for sample's acronym.

AC-K					
Cell condition	Circuit	R_1 [Ω]	R_2 [Ω]	$R=R_1+R_2$ [Ω]	χ^2
OCV	$R_e(R_1Q_1)(R_2Q_2)Q_g$	6.5 ± 1.4	26.6 ± 1.5	33.1± 2.9	4×10^{-5}
1 CV cycle	$R_e(R_1Q_1)(R_2Q_2)Q_g$	5.5 ± 0.7	15.8 ± 0.7	21.3 ± 1.4	2×10^{-5}
5 CV cycles	$R_e(R_1Q_1)(R_2Q_2)Q_g$	2.9 ± 0.7	39.6 ± 1.0	42.5 ± 1.7	4×10^{-5}
10 CV cycles	$R_e(R_1Q_1)(R_2Q_2)Q_g$	1.1 ± 0.3	76.5± 0.8	77.6 ± 1.1	4×10^{-5}
AC-H					
OCV	$R_e(R_1Q_1)Q_g$	2.9 ± 0.1	-	2.88 ± 0.1	2×10^{-4}
1 CV cycle	$R_e(R_1Q_1)Q_g$	23.5 ± 0.2	-	23.5 ± 0.2	8×10^{-5}
5 CV cycles	$R_e(R_1Q_1)Q_g$	32.3 ± 0.4	-	32.3 ± 0.4	7×10^{-5}
10 CV cycles	$R_e(R_1Q_1)Q_g$	39.5 ± 0.6	-	39.5 ± 0.6	5×10^{-5}

Hence, the characteristic electrode/electrolyte interphases in AC-K and AC-H is expected to influence the electrochemical response of the two materials both in lithium half-cell, and in lithium-ion full cell. Therefore, the applicability of the two electrodes is investigated in lithium cell galvanostatically cycled at different currents by adopting various protocols. Indeed, Figure 5 reports the cycling responses of AC-K (red curves), and AC-H (green curves) in lithium cell at a C/3 rate, and their rate capability at C/10, C/5, C/3, C/2, 1C, 2C and 5C (1C = 372 mA g^{-1}). Both AC-H and AC-K show during the initial 20 cycles a capacity decreasing from about 330 mAh g^{-1} to about 200 mAh g^{-1} (Fig. 5a). This trend, likely expected by progressive decomposition of the impurities in the two carbons, is reflected by the voltage profiles (Fig. 5c and Fig. 5e, respectively) which

significantly change from the 1st cycle (insets of the figures), to the 2nd, the 10th, and to the 20th cycle. Subsequently, the voltage trends of Fig. 5c and Fig. 4e reflect for both materials the typical sloping shape ascribed to the insertion of lithium into the disordered carbon below 1.2 V [68]. The above side processes initially depress the delivered capacity, and decrease the coulombic efficiency, which has a value below 50% during the first cycle (Fig. 5a); however, the processes leads also to the formation of a very stable interphase during the subsequent cycles [27] with an efficiency approaching 100%, and a reversible trend. This relevant stability is well justified by the inset of Fig. 5a which shows the trends of the electrode/electrolyte interphase resistance of the lithium half-cells using AC-K (red), and AC-H (green) upon the galvanostatic cycling at C/3 (see Figure S1 and Table S1 in the Supplementary Material for the corresponding Nyquist plots, and NLLS analyses). The data reveal a remarkable decrease of the overall electrode/electrolyte resistance for the cells, including both lithium anode, and either AC-K or AC-H, from about 48 Ω and 18 Ω, respectively, to low and constant values ranging between 7 and 9 Ω, thus further accounting for the electrode suitability for prolonged cycling. Hence, AC-H reveals a decrease of the specific capacity from about 200 at the 20th cycle to about 170 mAh g^{-1} upon 200 cycles, while AC-K shows a capacity slightly increasing, i.e., from 200 to about 210 mAh g^{-1}, upon the same number of cycles (Fig. 4a). The rate capability of the two samples in lithium cell is examined at the current of C/10, C/5, C/3, C/2, 1C, 2C and 5C (1C = 372 mA g^{-1}), and reported in terms of cycling trend (Fig. 5b), and voltage profile of selected cycles (Fig. 5d and Fig. 5f for AC-K and AC-H, respectively). The two samples evidence the initial decay already discussed above, and a different rate capability, with a higher delivered capacity for AC-H compared to AC-K at currents lower than C/2; accordingly, AC-H has an average capacity ranging from about 400 mAh g^{-1} at C/10 to 230 mAh g^{-1} at C/3, while AC-K shows an average value from about 320 mAh g^{-1} at C/10 to 200 mAh g^{-1} at C/3. This trend is reversed at C-rates higher than C/2, with an average capacity of AC-H ranging from about 120 mAh g^{-1} at 1C to 40 mAh g^{-1} at 5C for AC-H, and a value from about 140 mAh g^{-1} at 1C to 70 mAh g^{-1} at 5C for AC-K. The lower value of the capacity obtained at the higher currents is likely

attributed to the increase of the cell polarization, as evidenced by the voltage profiles of the rate capability tests reported in Fig. 5d and Fig. 5f for AC-K and AC-H, respectively. It is worth mentioning that the capacity values of AC-H, estimated by considering the carbon content only, i.e., by excluding 15 % of impurity observed above (see discussion of Fig. 1), may be actually higher than the ones observed in Fig. 5, thus further accounting for the differences observed between the two samples. Therefore, the difference observed between the two samples in terms of reversible capacity, and value of the electrode/electrolyte interphase resistance (Table 5) may be actually driven by the different nature of impurities, the textural properties, a greater BET surface of AC-H compared to the AC-K, the significant mesopore content interconnected with the micropores in AC-H, and the predominant presence of macroporous in with AC-K sample.

In overall, the galvanostatic tests in half-cell evidence the applicability of the two materials as the anode in Li-ion cell. However, the data of Fig. 5 suggest a preliminary treatment of the electrodes before use in full-cell in order to avoid the detrimental effect of the initial capacity decay, and achieve a suitable reversibility for an efficient application. In this respect, several procedures have been proposed, in particular for amorphous carbons and Li-alloy electrodes characterized by relevant irreversible capacity during the initial cycles [70–72]. Among them, electrochemical activation by pre-cycling of the electrodes in lithium half-cell [72], via surface modification and coatings [73], or by direct contact with lithium metal [70,71] evidenced the most suitable results in terms of stability of the full-cell. Therefore, prior to use AC-K and AC-H in full cell exploiting $LiFePO_4$ olivine-structure cathode [74] the two electrodes are electrochemically activated in half-cell by 30 galvanostatic cycles at C/3 to achieve the steady state observed in Fig. 5 (see experimental section for further details). The cells are balanced by slight anode excess with an N/P capacity ratio of about 1.03, according to the mass loading reported in the experimental section, considering the theoretical capacity of 170 mAh g^{-1} for $LiFePO_4$ (see corresponding cycling in half cell in Figure S2 in Supplementary Material) and a practical capacity at the steady state of about 200 mAh g^{-1} for the carbon electrodes.

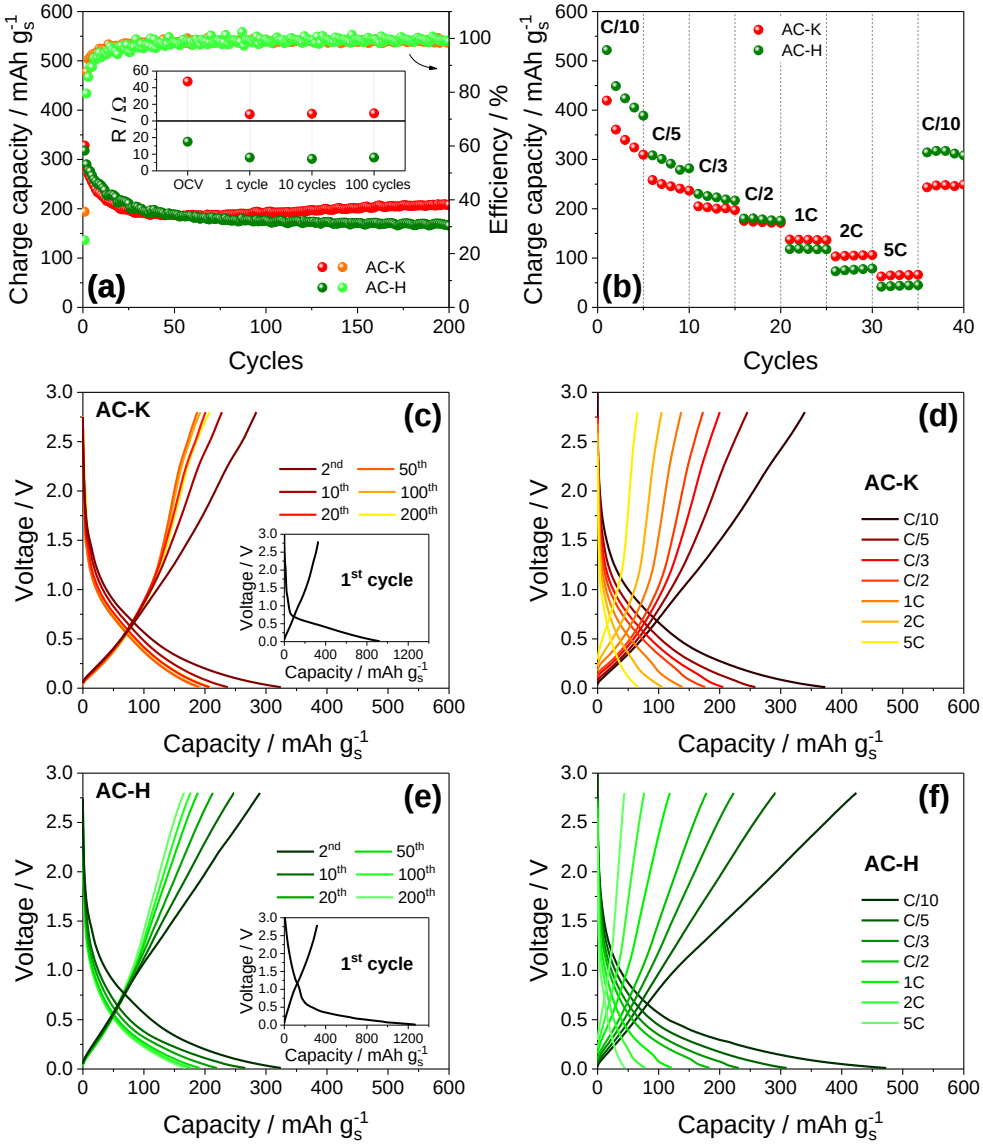

Figure 5. **(a-f)** Cycling performances of the electrodes in lithium half-cell. (**a**) Cycling trend with coulombic efficiency (right Y axis) of AC-K (red), and AC-H (green) in a lithium cell galvanostatically cycled at a C/3 rate (1C = 372 mA g^{-1}), and (**c**, **e**) corresponding voltage profiles, respectively, for selected cycles; inset in panel (a) shows the electrode/electrolyte interphase resistance values of the AC-K (red), and AC-H (green) measured by EIS upon the cycling at C/3 (see Figure S1 and Table S1 in the Supplementary Material for the corresponding Nyquist plots and NLLS analyses). (**b**) Rate capability cycling trend of AC-K (red), and AC-H (green) in a lithium cell galvanostatically cycled at C/10, C/5, C/3, C/2, 1C, 2C and 5C, and (**d**, **f**) corresponding voltage profiles, respectively, of selected cycles. Electrolyte: EC, DMC 1:1 (w/w), 1M $LiPF_6$. Voltage limits: 0.01-2.8 V. Temperature: 25 °C. See experimental section for sample's acronym.

Figure 6 reports the cycling performances of AC-K (red), and AC-H (green) in the lithium-ion full-cell, both at the constant c-rate of C/3 (1C = 170 mA g^{-1}) for evaluating the cycle life (Fig. 6a), and at various c-rates to determine the rate capability (Fig. 6b). After the initial few cycles characterized by some side irreversible processes dealing with electrolyte oxidation at the higher voltages, and possible reduction at the lower voltage values [75], the two cells remarkably deliver a steady state capacity of about 160 mAh g^{-1}, that is, a value of about 95% of the theoretical value of $LiFePO_4$. The corresponding voltage profiles, reported in Fig. 6c for AC-K, and Fig. 6e for AC-H, clearly evidence during the initial cycles the above mentioned processes likely occurring at about 3.6 V during charge and at 0.6 V during discharge. Furthermore, the steady state charge/discharge profile reflects the combination between the flat profile typical of the insertion process of the $LiFePO_4$ occurring at about 3.5 V vs. Li^+/Li [74], and the sloping one extending from about below 1.5 V until low potential of AC-K, and AC-H (compare with Fig. 5c, and Fig. 5e, respectively). Therefore, the cells show at the steady state a capacity approaching 160 mAh g^{-1} delivered with an average working voltage of about 2.8 V, thus a theoretical energy density of about 450 Wh kg^{-1} [1]. Remarkably, both cells evidence high efficiency after the initial cycles, and a relevant stability by the subsequent cycles (Fig. 6a). Hence, the cell using AC-K reveals a coulombic efficiency of about 98% (upon 20 cycles) leading to a capacity retention of 94% with respect to the steady state (160 mAh g^{-1}) upon 200 cycles, while the cell using AC-H shows after 20 cycles a coulombic efficiency higher than 99%, and a capacity retention as high as 96%. It is worth mentioning that the voltage shape of the cells (Fig. 6c for AC-K and Fig. 6e for AC-H) progressively modifies during cycles, in particular during the final stages of the test, likely due to a slight change of the cell balance promoted by the side processes, however without significant change of the delivered capacity [72]. The rate capability of the two full-cells is examined at currents increasing from C/5 to C/3, 1C and 2C (Fig. 6b). After the initial cycles at C/5 during which the cells undergo side reactions affecting the delivered capacity, the figure shows stable values of about 162, 159, 123, and 79 mAh g^{-1} for

the cell using AC-K, and 156, 148, 98, and 67 mAh g^{-1} for the cell using AC- H at C/5, C/3, 1C and 2C, respectively.

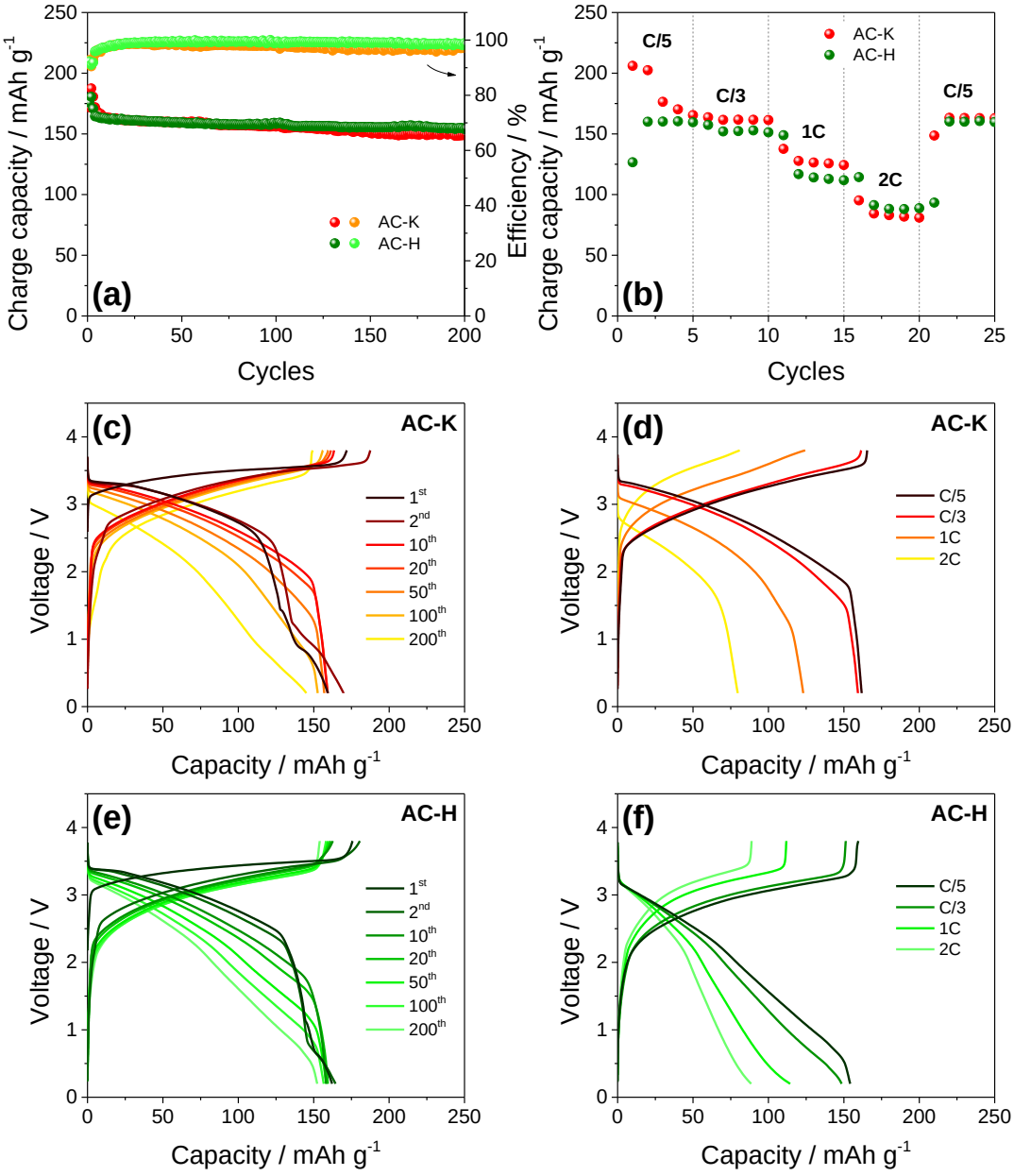

Figure 6. **(a-f)** Cycling performances of the electrodes in lithium-ion full-cell using a $LiFePO_4$ cathode. (**a**) Cycling trend with coulombic efficiency (right Y axis) of AC-K (red), and AC-H (green) in a lithium-ion cell galvanostatically cycled at a C/3 rate (1C = 170 mA g^{-1}), and (**c**, **e**) corresponding voltage profiles, respectively, for selected cycles. (**b**) Rate capability cycling trend of AC-K (red), and AC-H (green) in a lithium-ion cell galvanostatically cycled at C/5, C/3, 1C, and 2C, and (**d**, **f**) corresponding voltage profiles, respectively, of selected cycles. Electrolyte: EC,

DMC 1:1 (w/w), 1M $LiPF_6$. Voltage limits: 0.2-3.8 V. Temperature: 25 °C. See experimental section for sample's acronym.

Therefore, the cells show the expected decrease of the delivered capacity by raising the current due to the increase of the polarization (Fig. 6d, and Fig. 6f for AC-K, and AC-H, respectively), however with an excellent rate capability. Compared to the half-cells, the full cells using the two carbons reveal less differences, most likely due to the pre-activation process prior to cycling which mitigates the irreversible processes ascribed to the different samples' nature, and composition. Despite further insights may be required to fully setup the activation pathway of AC-K and AC-H for achieving a low impurity content, the remarkable performances of the lithium-ion cells reported above actually suggest the two electrodes as alternative anode materials for a safe, low cost, and environmentally sustainable energy storage.

4. Conclusions

Several literature papers reported carbons derived from bio masses for application as anode in lithium battery. Among them, loofah-derived pseudo-graphite (LPG) prepared through alkali treatment process followed by pyrolysis was used in Li-cell with specific capacity of 225 mAh g^{-1} after 200 cycles at the current density of 100 mA g^{-1} [25]. A carbonaceous material obtained by mechanochemical dry milling of spent coffee grounds (SCG), and carbonization at 800 C delivered in lithium cell initial specific capacity of 360 mAh g^{-1} current density of 0.1 A g^{-1}, and a reversible capacity of 285 mAh g^{-1} over 100 cycles [26]. Honey derived mesoporous nitrogen-doped carbons (HMNCs) showed a reversible capacity of about 700 mA h g^{-1} after 200 cycles at 1 A g^{-1} [27], while carbon nanofibers (CNFs) prepared by liquefying the biomass, electrospinning and carbonizing at high temperature exhibited a specific capacity of 272 mA h g^{-1} at 30 mA g^{-1}, good rate capability (131 and 102 mA h g^{-1} at 1 A g^{-1} and 2 A g^{-1}, respectively), and excellent cycling performance [28]. Disordered carbons obtained from cherry stones were tested as electrodes for lithium batteries up to 100 cycles from C/10 to 5C, with specific capacity of 200 mAh g^{-1} at 5C

[29]. Microtubular carbons obtained from bamboo and woods by acid treatment, and carbonization were used in lithium battery with capacity of 435 mA h g^{-1} at 50 mA g^{-1}, 150 mA h g^{-1} at 2 A g^{-1}, and 76% capacity retention at 500 mA g^{-1} upon 500 cycles [30]. Hard carbon from a natural gel derived from the Basil seeds (*Osimum Basilicum*) obtained by pyrolysis of the freeze- dried mucilage possesses sheet- like, showed a reversible capacity of 195 mAh g^{-1} at 0.1 A g^{-1} with 91 % retention after 300 cycles [31]. Three-dimensional (3D) rod-like carbon micro-structures derived from natural ramie fibers, and two-dimensional (2D) carbon nanosheets derived from corncobs prepared by heat treatment exhibited a capacity of 489 and 606 $mAhg^{-1}$ after 180 cycles at current density of 100 mAg^{-1} [32]. However, the good performances in terms of delivered capacity, cycle life and rate capability for large part of the above carbons were principally obtained in lithium half-cell rather than Li-ion full cell.

In our work, two carbon materials derived from cherry pit, and differing by the activation pathway have been fully characterized for application as the anode in Li-ion battery. The two materials revealed slightly different structure and morphology and, in particular, a different content and nature of the impurity depending on the adopted activation method. Indeed, the material treated by KOH (indicated by AC-K) revealed more relevant organic fraction, while the material activated by H_3PO_4 (indicated by AC-H) mostly showed an inorganic residual. The two samples have also shown significant differences of textural properties. AC-H sample evidenced a BET surface higher by 40% compared to AC-K, and a micro-/mesopore system rather than micro-/macropore one. These differences have been reflected into a characteristic electrochemical behavior in lithium cell, both in terms of the voltage shape, the rate capability, and of the delivered capacity. However, upon the initial irreversible cycles due to the above mentioned impurities, the two materials revealed very stable and reversible trends, whit steady state capacity approaching 200 mAh $g^{-1,}$ which suggested the applicability in lithium-ion full cell upon an electrochemical pre-treatment. Therefore, electrochemically pre-cycled AC-K and AC-H electrodes have been used in a full cell in combination with a $LiFePO_4$ electrode. The Li-ion cells delivered a very stable capacity

approaching the theoretical value of the cathode with a cycle life extended over 200 cycles, an efficiency approaching 100% upon the initial stage, a retention exceeding 90%, and a rate capability extending over 2C. Considering a cell capacity of 160 mAh g^{-1} and an average working voltage of about 2.8 V, the two cells delivered a theoretical energy density of about 450 Wh kg^{-1}, which may be actually reflected into a practical value exceeding 150 Wh kg^{-1}. These performances suggested the AC-K and AC-H materials as anodes for application in efficient Li-ion cell characterized by a remarkable stability, and a relevant environmental sustainability. However, the results also indicated that further work is needed in order to optimize the synthesis procedure to achieve high-purity carbons, and limit the effects of the side reactions during cell cycling.

Acknowledgements

This work was funded by the grant "Fondo per l'Incentivazione alla Ricerca (FIR) 2018", University of Ferrara, and performed within the collaboration project "Accordo di Collaborazione Quadro 2015" between University of Ferrara (Department of Chemical and Pharmaceutical Sciences) and Sapienza University of Rome (Department of Chemistry). Likewise, this research was funded by Ministerio de Economía y Competitividad (Project MAT2017-87541-R) and Junta de Andalucía (Group FQM-175).

References

[1] D. Di Lecce, R. Verrelli, J. Hassoun, Lithium-ion batteries for sustainable energy storage: Recent advances towards new cell configurations, Green Chem. 19 (2017) 3442–3467. doi:10.1039/c7gc01328k.

[2] C. McGlade, P. Ekins, The geographical distribution of fossil fuels unused when limiting global warming to 2 °C, Nature. 517 (2015) 187–190. doi:10.1038/nature14016.

[3] C.D. Thomas, A. Cameron, R.E. Green, M. Bakkenes, L.J. Beaumont, Y.C. Collingham, et al., Extinction risk from climate change, Nature. 427 (2004) 145–148.

doi:10.1038/nature02121.

[4] J. Xu, S. Dou, H. Liu, L. Dai, Cathode materials for next generation lithium ion batteries, Nano Energy. 2 (2013) 439–442. doi:10.1016/j.nanoen.2013.05.013.

[5] R. Van Noorden, The rechargeable revolution: A better battery, Nature. 507 (2014) 26–28. doi:10.1038/507026a.

[6] J. Xu, Y. Dou, Z. Wei, J. Ma, Y. Deng, Y. Li, et al., Recent Progress in Graphite Intercalation Compounds for Rechargeable Metal (Li, Na, K, Al)-Ion Batteries, Adv. Sci. 4 (2017). doi:10.1002/advs.201700146.

[7] M. Ashuri, Q. He, L.L. Shaw, Silicon as a potential anode material for Li-ion batteries: where size, geometry and structure matter, Nanoscale. 8 (2016) 74–103. doi:10.1039/C5NR05116A.

[8] A.R. Kamali, D.J. Fray, Tin-based materials as advanced anode materials for lithium ion batteries: A review, Rev. Adv. Mater. Sci. 27 (2011) 14–24.

[9] J. Hassoun, P. Ochal, S. Panero, G. Mulas, C. Bonatto Minella, B. Scrosati, The effect of CoSn/CoSn2 phase ratio on the electrochemical behaviour of Sn40Co40C20 ternary alloy electrodes in lithium cells, J. Power Sources. 180 (2008). doi:10.1016/j.jpowsour.2008.01.059.

[10] G.A. Elia, U. Ulissi, S. Jeong, S. Passerini, J. Hassoun, Exceptional long-life performance of lithium-ion batteries using ionic liquid-based electrolytes, Energy Environ. Sci. 9 (2016) 3210–3220. doi:10.1039/c6ee01295g.

[11] H.-G. Jung, M.W. Jang, J. Hassoun, Y.-K. Sun, B. Scrosati, A high-rate long-life Li4Ti5O12/Li[Ni0.45Co0.1Mn1.45]O4 lithium-ion battery, Nat. Commun. 2 (2011) 516. doi:10.1038/ncomms1527.

[12] T. Tsumura, A. Katanosaka, I. Souma, T. Ono, Y. Aihara, J. Kuratomi, et al., Surface modification of natural graphite particles for lithium ion batteries, Solid State Ionics. 135 (2000) 209–212. doi:10.1016/S0167-2738(00)00365-9.

[13] O.A. Vargas C., Á. Caballero, J. Morales, Can the performance of graphene nanosheets for lithium storage in Li-ion batteries be predicted?, Nanoscale. 4 (2012) 2083. doi:10.1039/c2nr11936f.

[14] R. Verrelli, J. Hassoun, High capacity tin–iron oxide-carbon nanostructured anode for advanced lithium ion battery, J. Power Sources. 299 (2015) 611–616. doi:10.1016/j.jpowsour.2015.09.034.

[15] R. Verrelli, J. Hassoun, High-Capacity NiO-(Mesocarbon Microbeads) Conversion Anode for Lithium-Ion Battery, ChemElectroChem. 2 (2015) 988–994. doi:10.1002/celc.201500069.

[16] C. Hernández-Rentero, O. Vargas, A. Caballero, J. Morales, F. Martín, Solvothermal-induced 3D graphene networks: Role played by the structural and textural properties on lithium storage, Electrochim. Acta. 222 (2016) 914–920. doi:10.1016/j.electacta.2016.11.057.

[17] R. Mo, F. Li, X. Tan, P. Xu, R. Tao, G. Shen, et al., High-quality mesoporous graphene particles as high-energy and fast-charging anodes for lithium-ion batteries, Nat. Commun. 10 (2019) 1–10. doi:10.1038/s41467-019-09274-y.

[18] D. Di Lecce, P. Andreotti, M. Boni, G. Gasparro, G. Rizzati, J.-Y. Hwang, et al., Multiwalled Carbon Nanotubes Anode in Lithium-Ion Battery with LiCoO 2 , Li[Ni 1/3 Co 1/3 Mn 1/3]O 2 , and LiFe 1/4 Mn 1/2 Co 1/4 PO 4 Cathodes, ACS Sustain. Chem. Eng. 6 (2018) 3225–3232. doi:10.1021/acssuschemeng.7b03395.

[19] L. Wang, X. Hu, Recent Advances in Porous Carbon Materials for Electrochemical Energy

Storage, Chem. - An Asian J. 13 (2018) 1518–1529. doi:10.1002/asia.201800553.

[20] J. Chen, C. Li, Z. Ristovski, A. Milic, Y. Gu, M.S. Islam, et al., A review of biomass burning: Emissions and impacts on air quality, health and climate in China, Sci. Total Environ. 579 (2017) 1000–1034. doi:10.1016/j.scitotenv.2016.11.025.

[21] L. Jiang, L. Sheng, Z. Fan, Biomass-derived carbon materials with structural diversities and their applications in energy storage, Sci. China Mater. 61 (2018) 133–158. doi:10.1007/s40843-017-9169-4.

[22] J. Jiang, K. Zhu, Y. Fang, H. Wang, K. Ye, J. Yan, et al., Coralloidal carbon-encapsulated CoP nanoparticles generated on biomass carbon as a high-rate and stable electrode material for lithium-ion batteries, J. Colloid Interface Sci. 530 (2018) 579–585. doi:10.1016/j.jcis.2018.07.019.

[23] C. Chen, Y. Huang, Y. Zhu, Z. Zhang, Z. Guang, Z. Meng, et al., Nonignorable Influence of Oxygen in Hard Carbon for Sodium Ion Storage, ACS Sustain. Chem. Eng. 8 (2020) 1497–1506. doi:10.1021/acssuschemeng.9b05948.

[24] P. Sennu, N. Arun, S. Madhavi, V. Aravindan, Y.-S. Lee, All carbon based high energy lithium-ion capacitors from biomass: The role of crystallinity, J. Power Sources. 414 (2019) 96–102. doi:10.1016/j.jpowsour.2018.12.089.

[25] Z. Wu, L. Wang, J. Huang, J. Zou, S. Chen, H. Cheng, et al., Loofah-derived carbon as an anode material for potassium ion and lithium ion batteries, Electrochim. Acta. 306 (2019) 446–453. doi:10.1016/j.electacta.2019.03.165.

[26] F. Luna-Lama, D. Rodríguez-Padrón, A.R. Puente-Santiago, M.J. Muñoz-Batista, A. Caballero, A.M. Balu, et al., Non-porous carbonaceous materials derived from coffee waste grounds as highly sustainable anodes for lithium-ion batteries, J. Clean. Prod. 207 (2019) 411–417. doi:10.1016/j.jclepro.2018.10.024.

[27] Y. Zhang, L. Chen, Y. Meng, J. Xie, Y. Guo, D. Xiao, Lithium and sodium storage in highly ordered mesoporous nitrogen-doped carbons derived from honey, J. Power Sources. 335 (2016) 20–30. doi:10.1016/j.jpowsour.2016.08.096.

[28] L. Tao, Y. Huang, X. Yang, Y. Zheng, C. Liu, M. Di, et al., Flexible anode materials for lithium-ion batteries derived from waste biomass-based carbon nanofibers: I. Effect of carbonization temperature, RSC Adv. 8 (2018) 7102–7109. doi:10.1039/c7ra13639k.

[29] J.C. Arrebola, A. Caballero, L. Hernán, J. Morales, V. Gómez-Serrano, Improving the Performance of Biomass-Derived Carbons in Li-Ion Batteries by Controlling the Lithium Insertion Process, J. Electrochem. Soc. 157 (2010) A791–A797. doi:10.1149/1.3425728.

[30] X. Zhang, J. Hu, X. Chen, M. Zhang, Q. Huang, X. Du, et al., Microtubular carbon fibers derived from bamboo and wood as sustainable anodes for lithium and sodium ion batteries, J. Porous Mater. (2019). doi:10.1007/s10934-019-00781-3.

[31] N. Sharma, Y. Gawli, A. Ahmad, M. Muhammed, S. Ogale, Nanotubular Hard Carbon Derived from Renewable Natural Seed Gel for High Performance Sodium-Ion Battery Anode, ChemistrySelect. 2 (2017) 6909–6915. doi:10.1002/slct.201701123.

[32] Q. Jiang, Z. Zhang, S. Yin, Z. Guo, S. Wang, C. Feng, Biomass carbon micro/nano-structures derived from ramie fibers and corncobs as anode materials for lithium-ion and sodium-ion batteries, Appl. Surf. Sci. 379 (2016) 73–82. doi:10.1016/j.apsusc.2016.03.204.

[33] A.A. Arie, B. Tekin, E. Demir, R. Demir-Cakan, Hard carbons derived from waste tea bag powder as anodes for sodium ion battery, Mater. Technol. 34 (2019) 515–524. doi:10.1080/10667857.2019.1586087.

[34] N. Moreno, A. Caballero, L. Hernán, J. Morales, Lithium–sulfur batteries with activated carbons derived from olive stones, Carbon N. Y. 70 (2014) 241–248. doi:10.1016/j.carbon.2014.01.002.

[35] A. Benítez, M. González-Tejero, Á. Caballero, J. Morales, Almond shell as a microporous carbon source for sustainable cathodes in lithium-sulfur batteries, Materials (Basel). 11 (2018) 1428. doi:10.3390/ma11081428.

[36] H. Chen, P. Xia, W. Lei, Y. Pan, Y. Zou, Z. Ma, Preparation of activated carbon derived from biomass and its application in lithium–sulfur batteries, J. Porous Mater. 26 (2019) 1325–1333. doi:10.1007/s10934-019-00720-2.

[37] M. Shahbandeh, Cherry production worldwide from 2000 to 2017, 2019-02-01. (2019). https://www.statista.com/statistics/577489/world-cherry-production/.

[38] Z. Li, Z. Xu, X. Tan, H. Wang, C.M.B. Holt, T. Stephenson, et al., Mesoporous nitrogen-rich carbons derived from protein for ultra-high capacity battery anodes and supercapacitors, Energy Environ. Sci. 6 (2013) 871–878. doi:10.1039/c2ee23599d.

[39] K. Hong, L. Qie, R. Zeng, Z. Yi, W. Zhang, D. Wang, et al., Biomass derived hard carbon used as a high performance anode material for sodium ion batteries, J. Mater. Chem. A. 2 (2014) 12733. doi:10.1039/C4TA02068E.

[40] J. Wang, S. Kaskel, KOH activation of carbon-based materials for energy storage, J. Mater. Chem. 22 (2012) 23710–23725. doi:10.1039/c2jm34066f.

[41] M.S. Solum, R.J. Pugmire, M. Jagtoyen, F. Derbyshire, Evolution of carbon structure in chemically activated wood, Carbon N. Y. 33 (1995) 1247–1254. doi:10.1016/0008-6223(95)00067-N.

[42] H.J. Denisa, A.M. Puziy, O.I. Poddubnaya, S.G. Fabian, J.M.D. Tascón, G.Q. Lu, Highly stable performance of supercapacitors from phosphorus-enriched carbons, J. Am. Chem. Soc. 131 (2009) 5026–5027. doi:10.1021/ja809265m.

[43] C. Hernández-Rentero, R. Córdoba, N. Moreno, A. Caballero, J. Morales, M. Olivares-Marín, et al., Low-cost disordered carbons for Li/S batteries: A high-performance carbon

with dual porosity derived from cherry pits, Nano Res. 11 (2018) 89–100. doi:10.1007/s12274-017-1608-1.

[44] F. Croce, A. D' Epifanio, J. Hassoun, A. Deptula, T. Olczac, B. Scrosati, A Novel Concept for the Synthesis of an Improved LiFePO[sub 4] Lithium Battery Cathode, Electrochem. Solid-State Lett. 5 (2002) A47. doi:10.1149/1.1449302.

[45] S. Wei, Z. Li, K. Kimura, S. Inoue, L. Pandini, D. Di Lecce, et al., Glyme-based electrolytes for lithium metal batteries using insertion electrodes: An electrochemical study, Electrochim. Acta. 306 (2019) 85–95. doi:10.1016/j.electacta.2019.03.051.

[46] M. Olivares-Marin, C. Fernandez-Gonzalez, A. Macias-Garcia, V. Gomez-Serrano, Preparation of activated carbons from cherry stones by activation with potassium hydroxide, Appl. Surf. Sci. 252 (2006) 5980–5983. doi:10.1016/j.apsusc.2005.11.018.

[47] M. Olivares-Marin, C. Fernandez-Gonzalez, A. Macias-Garcia, V. Gomez-Serrano, Porous structure of activated carbon prepared from cherry stones by chemical activation with phosphoric acid, Energy and Fuels. 21 (2007) 2942–2949. doi:10.1021/ef060652u.

[48] S. Brutti, J. Hassoun, B. Scrosati, C. Lin, H. Wu, H. Hsieh, A high power Sn-C/C-LiFePO4 lithium ion battery, J. Power Sources. 217 (2012) 72–76. doi:10.1016/j.jpowsour.2012.05.102.

[49] M.M. DUBININ, Physical Adsorption of Gases and Vapors in Micropores, in: D.A. Cadenhead, J.F. Danielli, M.D. Rosenberg (Eds.), Prog. Surf. Membr. Sci., Academic Press: New York, New York, 1975: pp. 1–70. doi:10.1016/b978-0-12-571809-7.50006-1.

[50] W. Ruland, B. Smarsly, X-ray scattering of non-graphitic carbon: an improved method of evaluation, J. Appl. Crystallogr. 35 (2002) 624–633. doi:10.1107/S0021889802011007.

[51] A.K. Kercher, D.C. Nagle, Microstructural evolution during charcoal carbonization by X-ray diffraction analysis, Carbon N. Y. 41 (2003) 15–27. doi:10.1016/S0008-6223(02)00261-0.

[52] G.A. Zickler, B. Smarsly, N. Gierlinger, H. Peterlik, O. Paris, A reconsideration of the relationship between the crystallite size La of carbons determined by X-ray diffraction and Raman spectroscopy, Carbon N. Y. 44 (2006) 3239–3246. doi:10.1016/j.carbon.2006.06.029.

[53] M. Jagtoyen, F. Derbyshire, Activated carbons from yellow poplar and white oak by H3PO4 activation, Carbon N. Y. 36 (1998) 1085–1097. doi:10.1016/S0008-6223(98)00082-7.

[54] A. Kumar, H.M. Jena, Preparation and characterization of high surface area activated carbon from Fox nut (Euryale ferox) shell by chemical activation with H 3 PO 4, Results Phys. 6 (2016) 651–658. doi:10.1016/j.rinp.2016.09.012.

[55] F. Quesada-Plata, R. Ruiz-Rosas, E. Morallón, D. Cazorla-Amorós, Activated Carbons Prepared through H 3 PO 4 -Assisted Hydrothermal Carbonisation from Biomass Wastes: Porous Texture and Electrochemical Performance, Chempluschem. 81 (2016) 1349–1359. doi:10.1002/cplu.201600412.

[56] F. Yu, S. Li, W. Chen, T. Wu, C. Peng, Biomass- Derived Materials for Electrochemical Energy Storage and Conversion: Overview and Perspectives, ENERGY Environ. Mater. 2 (2019) 55–67. doi:10.1002/eem2.12030.

[57] J. Wang, P. Nie, B. Ding, S. Dong, X. Hao, H. Dou, et al., Biomass derived carbon for energy storage devices, J. Mater. Chem. A. 5 (2017) 2411–2428. doi:10.1039/C6TA08742F.

[58] D. Aurbach, B. Markovsky, G. Salitra, E. Markevich, Y. Talyossef, M. Koltypin, et al., Review on electrode-electrolyte solution interactions, related to cathode materials for Li-ion batteries, J. Power Sources. 165 (2007) 491–499. doi:10.1016/j.jpowsour.2006.10.025.

[59] P. Verma, P. Maire, P. Novák, A review of the features and analyses of the solid electrolyte interphase in Li-ion batteries, Electrochim. Acta. 55 (2010) 6332–6341. doi:10.1016/j.electacta.2010.05.072.

[60] M. Winter, J.O. Besenhard, M.E. Spahr, P. Novák, Insertion electrode materials for

rechargeable lithium batteries, Adv. Mater. 10 (1998) 725–763. doi:10.1002/(SICI)1521-4095(199807)10:10<725::AID-ADMA725>3.0.CO;2-Z.

[61] M.B. Pinson, M.Z. Bazant, Theory of SEI Formation in Rechargeable Batteries: Capacity Fade, Accelerated Aging and Lifetime Prediction, J. Electrochem. Soc. 160 (2013) A243–A350. doi:10.1149/2.044302jes.

[62] C.J. Wen, C. Ho, B. a. Boukamp, I.D. Raistrick, W. Weppner, R. a. Huggins, Use of electrochemical methods to determine chemical-diffusion coefficients in alloys: application to 'LiAI,' Int. Mater. Rev. 26 (2012) 253–268. doi:10.1179/095066081790149195.

[63] C. Ho, I.D. Raistrick, R.A. Huggins, Application of A-C Techniques to the Study of Lithium Diffusion in Tungsten Trioxide Thin Films, J. Electrochem. Soc. 127 (1980) 343–350. doi:10.1149/1.2129668.

[64] D. Aurbach, M.D. Levi, E. Levi, A review on the solid-state ionics of electrochemical intercalation processes: How to interpret properly their electrochemical response, Solid State Ionics. 179 (2008) 742–751. doi:10.1016/j.ssi.2007.12.070.

[65] B.A. Boukamp, A package for impedance/admittance data analysis, Solid State Ionics. 18–19 (1986) 136–140. doi:10.1016/0167-2738(86)90100-1.

[66] D. Di Lecce, R. Verrelli, D. Campanella, V. Marangon, J. Hassoun, A New CuO-Fe2O3-Mesocarbon Microbeads Conversion Anode in a High-Performance Lithium-Ion Battery with a Li1.35Ni0.48Fe0.1Mn1.72O4 Spinel Cathode, ChemSusChem. 10 (2017) 1607–1615. doi:10.1002/cssc.201601638.

[67] D. Aurbach, Review of selected electrode–solution interactions which determine the performance of Li and Li ion batteries, J. Power Sources. 89 (2000) 206–218. doi:10.1016/S0378-7753(00)00431-6.

[68] E. Buiel, J.R. Dahn, Li-insertion in hard carbon anode materials for Li-ion batteries,

Electrochim. Acta. 45 (1999) 121–130. doi:10.1016/S0013-4686(99)00198-X.

[69] S.L. Candelaria, Y. Shao, W. Zhou, X. Li, J. Xiao, J.G. Zhang, et al., Nanostructured carbon for energy storage and conversion, Nano Energy. 1 (2012) 195–220. doi:10.1016/j.nanoen.2011.11.006.

[70] J. Hassoun, K.S. Lee, Y.K. Sun, B. Scrosati, An advanced lithium ion battery based on high performance electrode materials, J. Am. Chem. Soc. 133 (2011) 3139–3143. doi:10.1021/ja110522x.

[71] G.A. Elia, J. Wang, D. Bresser, J. Li, B. Scrosati, S. Passerini, et al., A new, high energy Sn-C/Li[Li0.2Ni0.4/3Co 0.4/3Mn1.6/3]O2 lithium-ion battery, ACS Appl. Mater. Interfaces. 6 (2014) 12956–12961. doi:10.1021/am502884y.

[72] D. Di Lecce, S. Levchenko, F. Iacoviello, D.J.L. Brett, P.R. Shearing, J. Hassoun, X- ray Nano- computed Tomography of Electrochemical Conversion in Lithium- ion Battery, ChemSusChem. (2019) cssc.201901123. doi:10.1002/cssc.201901123.

[73] D. Molina Piper, S.-B. Son, J.J. Travis, Y. Lee, S.S. Han, S.C. Kim, et al., Mitigating irreversible capacity losses from carbon agents via surface modification, J. Power Sources. 275 (2015) 605–611. doi:10.1016/j.jpowsour.2014.11.032.

[74] A. Eftekhari, LiFePO 4 /C nanocomposites for lithium-ion batteries, J. Power Sources. 343 (2017) 395–411. doi:10.1016/j.jpowsour.2017.01.080.

[75] J. Vetter, P. Nov??k, M.R. Wagner, C. Veit, K.C. M??ller, J.O. Besenhard, et al., Ageing mechanisms in lithium-ion batteries, J. Power Sources. 147 (2005) 269–281. doi:10.1016/j.jpowsour.2005.01.006.

Unmarked Revised manuscript
Click here to view linked References

Alternative Lithium-Ion Battery Using Biomass-Derived Carbons as Environmentally Sustainable Anode

Celia Hernández-Rentero[1], Vittorio Marangon[2], Mara Olivares-Marín[3], Vicente Gómez-Serrano[3], Álvaro Caballero[1], Julián Morales[1]* and Jusef Hassoun[2]*

[1] Department of Química Inorgánica e Ingeniería Química, Instituto de Química Fina y Nanoquímica, University of Córdoba, 14071 Córdoba, Spain

[2] Department of Chemical and Pharmaceutical Sciences, University of Ferrara, Via Fossato di Mortara 17, Ferrara 44121, Italy

[3] Department of Química Inorgánica, Facultad de Ciencias, University of Extremadura, 06006 Badajoz, Spain

*Corresponding Authors. Tel: +39 0532-455163, E-mail: jusef.hassoun@uniroma1.it (Jusef Hassoun), Tel: +34 957218620, E-mail: iq1mopaj@uco.es (Julián Morales)

Abstract

Disordered carbons derived from biomass are herein efficiently used as an alternative anode in lithium-ion battery. Carbon precursor obtained from cherry pit is activated by using either KOH or H_3PO_4, to increase the specific surface area and enable porosity. Structure, morphology and chemical characteristics of the activated carbons are investigated by X-ray diffraction (XRD), transmission electron microscopy (TEM), scanning electron microscopy (SEM), thermogravimetry (TG), Raman spectroscopy, nitrogen and mercury porosimetry. The electrodes are studied in lithium half-cell by galvanostatic cycling, cyclic voltammetry, and electrochemical impedance spectroscopy (EIS). The study evidences substantial effect of chemical activation on the carbon morphology, electrode resistance, and electrochemical performance. The materials reveal the typical profile of disordered carbon with initial irreversibility vanishing during cycles. Carbons

activated by H_3PO_4 show higher capacity at the lower c-rates, while those activated by KOH reveal improved reversible capacity at the high currents, with efficiency approaching 100% upon initial cycles, and reversible capacity exceeding 175 mAh g^{-1}. Therefore, the carbons and $LiFePO_4$ cathode are combined in lithium-ion cells delivering 160 mAh g^{-1} at 2.8 V, with a retention exceeding 95% upon 200 cycles at C/3 rate. Hence, the carbons are suggested as environmentally sustainable anode for Li-ion battery.

1. Introduction

Lithium-ion battery is the most diffused energy storage system for modern applications such as computers, electronic devices, and electric vehicles (EVs) [1]. This important system may actually satisfy the increasing demand for energy storage from renewable sources for mitigating climate change issues, which are possibly driven from the use of fossil fuels, and related greenhouse gasses emission [2,3]. Lithium-ion battery, in its most conventional configuration, is formed by electrodes based on Li^+ intercalation or insertion materials at the cathode, such as $LiCoO_2$ and $LiFePO_4$, and graphite at the anode side, separated by an inorganic electrolyte dissolving a lithium salt (e.g., EC:DMC, $LiPF_6$) [1,4]. Since first commercialization by Sony Corporation during 1991[5] LIB employs graphite as the preferred anode, with a theoretical specific capacity of 372 mAh g^{-1} [6], while only few other examples of practical interest, such as Si and Sn-based materials [7,8], carbon/alloy mixtures [9,10], and lithium titanate spinel oxide [11] have been proposed as alternative materials. A great number of studies has focused on various carbonaceous materials alternative to graphite for application as anodes in LIBs [12–18]. Suitable characteristics for enabling the energy storage properties of carbons are an increased active surface area for ensuring sufficient contact between electrode and electrolyte, the presence of pores, and their size distribution. The latter characteristic plays a key role for enhancing the electrochemical process since micro-pores can fasten ions exchange, whereas the meso- and macro-pores act as a reservoir for active ions [19]. Furthermore, an increased awareness for environmental issues driven from CO_2

emission by biomass burning promoted several efforts for entrapping C in sustainable materials [20]. Therefore, biomass-derived carbon electrodes have attracted relevant attention due their structural versatility, tunable physical/chemical properties, environmental friendliness, and considerable economic value [21]. These substrates were actually employed in various energy-storage systems such as Li-ion, Na-ion and supercapacitors. Indeed, a recent paper reported ultrafine CoP nanoparticles embedded in carbon nanorod grown on the biomass-derived carbon (BC), that is, CoP@C/BC, as anode materials for lithium-ion batteries with a specific capacity of about 300 mAh g^{-1}, and an outstanding long-term cycling performance of about 1000 cycles [22]. Another effective method employed buckwheat hulls as the precursor to prepare oxygen-doped hard carbon by simple carbonization [23]. The electrode reveled in sodium battery a maximum reversible capacity of 400 mA h g^{-1} at 50 mA g^{-1}, and capacity retention of 96% with respect to the initial capacity (about 110 mAh g^{-1}) over 3000 cycles at 2A g^{-1}. Furthermore, all carbon-based Li-ion capacitor was obtained from environmentally threatening prosopis juliflora [24]. The pyrolyzed carbon exhibited a few layers of graphene-like structure, and tubular morphology with multiple inherent heteroatoms like N, S, and Ca which enhanced electrical conductivity, pore generation, thus improving capacity/capacitance of carbonaceous materials. The material has been lithiated, and it delivered an energy density of about 216 Wh kg^{-1}, retaining about 94% initial capacity after 5000 cycles [24]. Various carbons, obtained from loofah [25], coffee [26], honey [27], walnut shells [28], and cherry pits [29] residues, have been already reported as suitable electrode for lithium-ion battery, while other activated carbons derived from bamboo [30], natural seed [31], corncobs [32] or tea [33] residues have also been proposed for sodium batteries. In addition, olive stone [34], almond shell [35], walnut shell, peanut shell, and pistachio hull [36], have been used as precursor for carbons employed in Li-S batteries.

Herein, we propose an alternative carbon electrode obtained from the ligno-cellulosic waste of cherry pits (CP), which is considered a viable raw material since produced by a relevant amount (e.g., with global production of cherry in 2017 of about 2.5 millions of tons mainly used for Kirsch,

beers, jams, chocolates, manufacturing [37]). Generally, carbonaceous substrates obtained from bio-residues require an activation procedure involving chemical agents, such as bases (e.g., KOH) or acids (e.g., H_3PO_4), and thermal steps (e.g., annealing under Ar, Ar/H_2 or N_2 atmosphere), for removing organic fractions and promoting carbon porosity and surface characteristics suitable for application in battery [27,28,32,38,39]. In particular, potassium hydroxide (KOH) favors chemical activation according to a complex mechanism involving the formation of K_2CO_3, K_2O, and possibly reducing species such as metallic K, while thermal treatment generally produce water vapor, CO_2, and CO gasses leading to a physical activation [40]. Furthermore, phosphoric acid (H_3PO_4) can generate P-containing functional groups into the carbon matrix [41], which may promote the formation of micro-pores into the carbon, and actually improve the electrochemical stability of the material in battery [42]. We have previously shown the possible application of a carbon derived from cherry pits biomass activated by H_3PO_4 as a substrate in lithium-sulfur battery [43]. In this work, we extend our study by reporting carbons obtained from cherry pits, activated both by H_3PO_4 and KOH, and differing by the porosity nature and degree, for application in an alternative Li-ion battery using the $LiFePO_4$ cathode. $LiFePO_4$ is an olivine-structure materials characterized by a flat plateau at 3.5 V, a theoretical specific capacity of 170 mAh g^{-1}, and a relevant stability in lithium cell [44,45]. The carbon materials are fully characterized in terms of structure, morphology, and electrochemical behavior, and efficiently used in full cells characterized by an extended cycle life and a remarkable environmental compatibility.

2. Experimental section

2.1 *Synthesis of the active materials*

The two samples studied in this work were derived from biomass residues of cherry pits (CP), supplied by Asociación de Cooperativas del Valle del Jerte (Cáceres province, Spain). After being dried, and ground, the biomass residues of cherry pits (i.e., a sample still not suitable for battery testing due to the organic residue) were sized and the fraction of particle between 1 and 2 mm was

chosen. 50 g of residues were immersed in 250 mL of diluted H_2SO_4 solution (5 vol.%) for 24 h, filtered, and washed with distilled water until pH reached a value of 6 in the residual liquid. The resulting powder (CP) was processed according to previous reports, as summarized in Table 1. Accordingly, two different activation agents (AA), that is, potassium hydroxide (KOH) [46] (sample AC-K) and phosphoric acid (H_3PO_4) [47] (sample AC-H) were used. 25 g of powder were dispersed in distilled water, and added by the specific amount (Table 1) of either H_3PO_4 (85wt.% in H_2O, 99.99%, Sigma Aldrich) or KOH (ACS reagent, ≥85%, pellets, Sigma Aldrich). Subsequently, the samples were dried for 24 h at 100 °C, annealed for 2 h at 800 °C under N_2 atmosphere with a flow of 100 mL/min and heating rate of 10 °C/min, washed with diluted HCl, with distilled water until a pH value above 6, and finally dried in oven at 120 °C overnight.

The $LiFePO_4$ material was described a previous paper [48].

Table 1. Synthesis conditions of the activated carbons reported in this work

Sample acronym	Activation Agent (AA)	Preparation			
		CP (g)	AA (g)	T_C (°C)	t (h)
AC-H	H_3PO_4	25	44	800	2
AC-K	KOH	25	25	800	2

2.2 *Materials characterization*

The elemental chemical analysis of activated carbons was carried out using a LECO CHNS-932 micro-analyser coupled with a VTF900 furnace for oxygen. The system enables the analysis of carbon, hydrogen, nitrogen, and sulfur separately from oxygen. The structural properties were examined using XRD, Raman and FT-IR spectroscopy. The XRD patterns were obtained with a Bruker D8 Discover X-ray diffractometer, using CuKα radiation, and a Ge monochromator within a range of 2-80˚ (2θ) using a step size of 0.04° and 1.05 s per step. Raman measurements were performed under ambient conditions through a Renishaw inVia Microscope equipped with a Renishaw CCD Camera (578 x 400) detector, and a 532 nm edge in line focus mode laser. The FT-

IR spectra were recorded in a Perkin-Elmer 1720 FT-IR spectrometer in the 4000–400 cm^{-1} wavenumber range, 40 scans being taken at 2 cm^{-1} resolution. Pellets were prepared by mixing powdered sample, and KBr (Merck, for spectroscopy) at a sample/KBr weight ratio of 1:500. Each mixture was compacted at 10 tonnes cm^{-1} for 3 min, using a Perkin-Elmer hydraulic press.

The textural properties were examined by nitrogen, and mercury porosimetry. Autosorb-1 semiautomatic apparatus (Quantachrome) using nitrogen as an adsorbent was used to obtain the micropore volume (V_{mi}), by applying the Dubinin–Radushkevich equation [49]. The pore size distribution of the carbons in the micropore and narrow mesopore ranges was obtained by applying the density functional theory (DFT) method. Macropore, and mesopore volumes were determined by a mercury porosimeter Autoscan-60 (Quantachrome). From the plots of cumulative pore volume (V_{cu}) versus pore radius (r), macropore volume, $V_{ma} = V_{cu}$ (at r = 250 Å), and mesopore volume, $V_{me} = V_{cu}$ (at r < 20 Å) – V_{ma}, of the samples were obtained. Finally, the total pore volume (V_T) was estimated by using of the equation $V_T = V_{mi} + V_{me} + V_{ma}$.

Thermogravimetric analysis (TGA) was performed by using a Mettler Toledo TGA/DSC-1 at a heating rate of 10 °C min^{-1} from 30 to 800 °C, under an oxygen atmosphere. Before the measurements, the samples were dried overnight at 120ºC to remove traces of moisture.

Sample's morphology was studied by transmission electron microscopy (TEM), using a Zeiss EM 910 microscope equipped with a tungsten thermoionic electron gun operating at 100 kV, and scanning electron microscopy (SEM), using a Zeiss EVO 40 microscope equipped with a LaB_6 thermoionic electron gun. Energy-dispersive X-ray spectroscopy (EDS) was recorded on the SEM images through a X-ACT Cambridge Instruments analyzer to study the element distribution.

2.3 *Electrode preparation and electrochemical characterization*

The electrodes were prepared by mixing the active material, either carbons or $LiFePO_4$, with carbon super P (Timcal, conducting agent) and polyvinylidene fluoride (PVDF 6020, Solef Solvay, binder) in a weight proportion of 80:10:10, and adding 1-methyl-2-pyrrolidinone (NMP, Sigma-Aldrich) to

obtain a slurry for coating the electrode material on a Cu foil (MTI, 18μm) (carbons) or Al foil ($LiFePO_4$), using Doctor-Blade technique. The slurry was heated for 3 h at 70˚C by using a hot plate to remove the solvent, and finally cut into disks (either 10 or 14mm diameter), which were dried at 105˚C overnight under vacuum. The loading of the active material in the final electrode was about 3,5 mg cm^{-2} for carbons and 4 mg cm^{-2} for $LiFePO_4$.

The electrochemical process of the carbon materials was evaluated both in 2032 coin-type cells and 3-electrode T-cell, prepared in an Ar-filled glove box (MBraun, O_2 and H_2O content below 1 ppm), with a Li/ EC, DMC 1:1 (w/w), 1 M $LiPF_6$/carbon configuration, using the selected carbon as the working electrode (14 mm-diameter in coin cell and 10 mm-diameter in T-cell), a Whatman disk soaked with the electrolyte as the separator, and a lithium metal disk as the counter and reference electrode.

Cyclic voltammetry (CV) and Electrochemical impedance spectroscopy (EIS) tests were performed by using 3-electrode T-cell through a VersaSTAT MC Princeton Applied Research (PAR) analyzer. CV measurements consisted of ten cycles in the 0.01–2.8 V range with a scan rate of 0.1 mV s^{-1}, while EIS measurements were taken at the open circuit (OCV), after the first, fifth, and tenth CV cycle in the 500 kHz–100 mHz frequency range using a 10 mV signal amplitude.

Galvanostatic cycling tests were performed in coin-type cells by using a MACCOR series 4000 battery test system within the potential window 0.01–2.8 V. Rate Capability measurement was performed using current values of C/10, C/5, C/3, C/2, 1C, 2C and 5C (1C = 372 mAg^{-1}). Galvanostatic tests prolonged to 200 cycles were performed at constant rate of C/3. Both specific current and specific capacity were referred to the carbon mass, that is, the electrochemically active component in the electrode.

The stability of the two carbon materials in lithium cell upon prolonged galvanostatic cycling at C/3 (1C = 372 mA g^{-1}) was evaluated by performing EIS measurements at the OCV, and after the first,

tenth, and hundredth discharge/charge cycle in the 500 kHz–100 mHz frequency range using a 10 mV signal amplitude.

The performance of the $LiFePO_4$ cathode in lithium cell was investigated by a galvanostatic cycling test using a constant current rate of C/3 (1C = 170 mA g^{-1}) for over 100 cycles in the 2.7–4.0 V range. The cell was assembled by adopting the Li / EC, DMC 1:1 (w/w), 1 M $LiPF_6$ / $LiFePO_4$ configuration, using a Celgard separator soaked with the electrolyte. Both specific current and specific capacity were referred to the $LiFePO_4$ mass.

The lithium-ion full cells were assembled by coupling the selected carbon (either AC-K or AC-H) with a $LiFePO_4$ cathode in 2032 coin-type cells using the configuration Carbon/EC, DMC 1:1 (w/w), 1 M $LiPF_6$ /$LiFePO_4$. Before use in Li-ion cell, the carbon electrodes were pre-activated by 30 galvanostatic cycles in lithium half-cell at a current rate of C/3 (1C = 372 mA g^{-1}) in a coin cell with the above mentioned configuration. After activated, the carbon electrodes were washed using DMC, dried under vacuum for 30 min, and employed in the above described Li-ion cell as the negative electrode.

Cycling tests of the Li-ion cells were performed using a MACCOR series 4000 battery test system within the potential window 0.2–3.8 V. Rate capability measurements were performed using current values of C/5, C/3, 1C and 2C (1 C = 170 mA g^{-1}). Galvanostatic tests prolonged over 200 cycles were performed at a current rate of C/3. Both specific current and specific capacity of the full-cell were referred to the $LiFePO_4$.

3. Result and discussion

Coals composition is detected by elemental analysis and reported in terms of weight % in Table 2. The carbon activated with KOH reveals higher content of C (about 89%), less O (about 8%) and H (about 1%), compared to the sample activated by H_3PO_4 (about 81%, 11% and 2%, respectively), while N and S contents appear almost negligible for both samples (i.e., lower than 1%). Relevantly,

AC-K evidences an overall element content higher than 99%, instead AC-H shows an elemental content of about 94%, thus suggesting the additional presence of different atoms in the latter carbon. X-ray energy dispersive spectroscopy (EDS) of the AC-H sample reported subsequently (see Fig. 3) indicates phosphorous (P) as that the additional element (around 6% weight) by.

Table 2. Elemental analysis of AC-K and AC-H samples: weight % of C, H, N, S and O, respectively.

Sample	C	H	N	S	O	Sum
AC-K	88.99	1.05	0.65	0.05	8.34	99.08
AC-H	80.57	2.0	0.18	0.06	11.40	94.21

The structural characteristics of the carbon samples investigated in this work are summarized in Figure 1. Indeed, Fig. 1a shows the XRD patterns of AC-K (red line) and AC-H (green line) as well as the reference patterns of graphite (PDF # 41-1487). The figure evidences for both samples similar patterns characterized by the absence of defined peaks of ordered graphite, while the presence of two weak and broad signals around $2\theta = 26^{o}$ and 44^{o}, which can be likely attributed to the (0 0 2) and (1 0 0) reflections of highly disordered carbons [50,51]. Furthermore, the Raman spectra of Fig. 1b show the D and G bands of carbon at approximately $\tilde{\nu}$=1346 and 1594 cm^{-1}, respectively, with an intensity ratio (I_D/I_G) of 0.96 in AC-K and 0.95 in AC-H. The relatively high I_D/I_G value likely indicates a pronounced defect content and a small average size of the sp^2 domains [52]. It is worth mentioning that the slightly lower intensity of the XRD reflections and higher I_D/I_G value of the AC-K sample may likely suggest a more effective activation the carbon sample by using KOH rather than H_3PO_4 [42,43,46,47]. Relevantly, the TGA curves performed under oxygen and reported in Fig. 1c reveal a different trend for the two studied carbons. The two samples begin losing weight from about 200 °C, most likely due to organic residues which are more relevant in AC-K (about 18 % of weight loss until 450 °C) compared to AC-H (about 7% weight loss until 450

°C). Both samples reveal a fast decay of the weight around 500 °C due to the full oxidation of the carbon to CO_2. However, this pronounced weight loss represents more than 95% in the sample activated with KOH and only 40% when the activation is carried out with H_3PO_4. Therefore, the weight loss of the AC-H sample at temperatures higher than 500 °C may be likely ascribed to acid impurities rather than the exclusive pyrolysis of C. The inset of Fig. 1c, reporting the DTG curves, evidences at least two stages of weight loss for AC-H (green curve), that is, just above 500 °C and at about 650 °C, while only the main peak around 500 °C for AC-K (red curve). Lignocellulosic materials react with H_3PO_4 according to a complex bond-breaking process involving CO, CO_2 and CH_4 gases evolution, even at low temperatures, with formation of phosphate esters by cellulose phosphorylation [53]. On the other hand, appreciable presence of P is actually suggested by EDS hereafter, while the presence of phosphorylated functional groups is confirmed by the FT-IR spectra of the AC-H sample reported in Fig. 1d. The latter figure shows the absorption spectra of carbon samples activated using H_3PO_4 by heating at various temperatures between 350 and 550 ºC, that is, temperature range corresponding to the change of TG curve's slope observed in Fig. 1c. The FT-IR spectra reveal a series of shoulders and absorption bands whose position and allocation are detailed in Table 3 [54].

Table 3. Assignment of absorption bands of the FT-IR spectra of AC-H sample (cm^{-1}) collected in Fig. 1d.

Wavenumber / cm^{-1}	Assignments	Group
3388	ν (O−H)	Intermolecular hydrogen bond: alcohols, phenols and carboxylic acids
1693	ν (C=O)	Esters: quinone and carboxylic acids
1577	ν (C=C)	Olefinic groups and aromatic rings
1175	ν (C−OH)	Phenols and carboxylic acids
	ν (C−O) in C−O−C	Ethers

	ν (P=O)	Phosphate esters and polyphosphate
1001	ν (P−OH)	Phosphate esters and polyphosphate
	ν (C−O) in P-O-C	Phosphate esters and polyphosphate
912	ν (P−O) in P-O-C	Phosphate esters and polyphosphate

As above mentioned, elemental analysis (see Table 2) and EDS suggest for the carbons surface groups involving both O and P, despite the repeated washing adopted to leach the phosphorus species. Interestingly, the relative intensity of the IR bands located between 1600 and 1200 cm^{-1} (Fig. 1d) tends to increase by raising the temperature from 350 and 500 °C, thus suggesting increased concentration of surface groups with C= C, C─O and/ or P = O bonds, while a further temperature raise leads to the decrease of the functional groups content. Therefore, the weight loss at temperature higher than 500 °C observed by thermogravimetry (Fig. 1c) would mainly correspond to the gasification of carbon, while at higher temperatures additional phases related to the phosphorous groups would also be volatilized, thus accounting for the AC-H thermogram complexity observed in Fig. 1c.

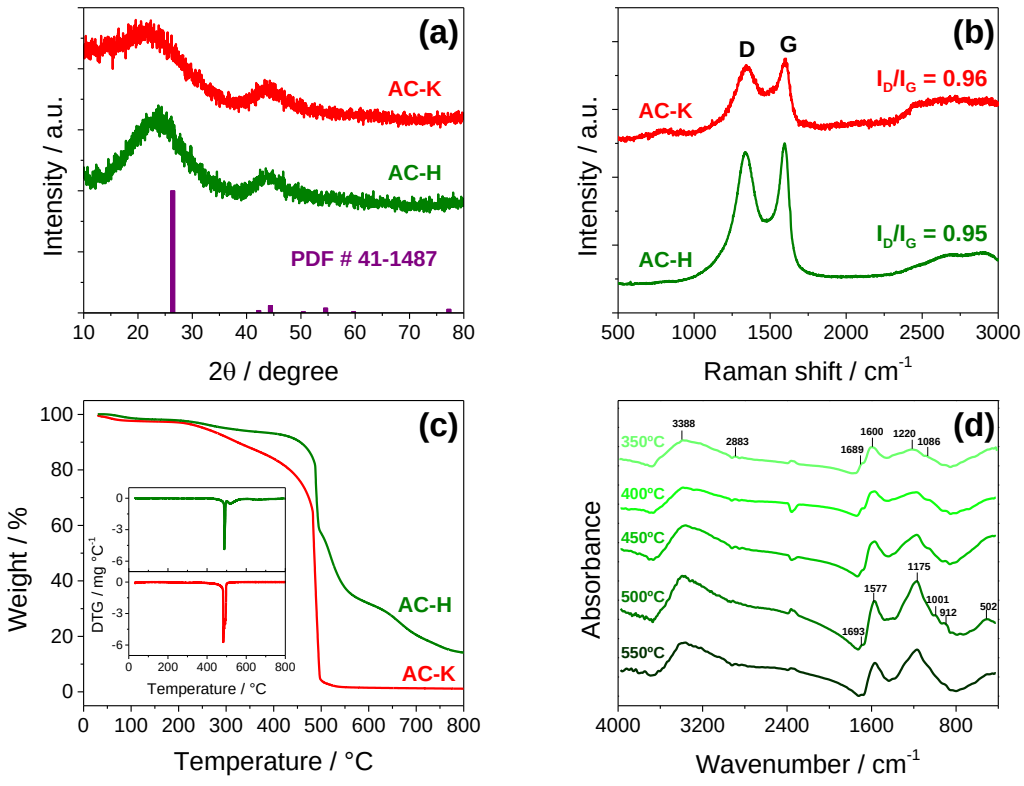

Figure 1. **(a-c)** Structural study of the samples**.** (**a**) X-ray diffraction patterns (XRD), (**b**) Raman spectra, (**c**) Thermogravimetric Analysis (TGA) under oxygen atmosphere of AC-K (red line) and AC-H (green line); (insert: DTG curves) **(d)** FT-IR spectra of the AC-H sample heated at different temperatures. See experimental section for sample's acronym.

The high ash content in AC-H, around 15%, is also observed in other biomass-derived carbons activated with H_3PO_4 [55] in a much higher ratio than samples activated by KOH such as AC-K. Therefore, the thermal measurements reveal substantial differences between the two sample, and likely suggest a more relevant organic fraction for AC-K while a more significant inorganic residue for AC-H.

The effects of the activation conditions on the surface area and the pore volume of the two samples are evaluated by N_2 and Hg adsorption-desorption measurements reported in Figure 2 and summarized in Table 4. The N_2 adsorption isotherms of the two activated carbons shown in Fig. 2a reveal the expected trends, both belonging to a type I BDDT classification, typical of microporous solids with relatively small external surfaces. The higher adsorption values of the sample AC-H with respect to AC-K observed in Fig. 2a indicate extended surface area of the former compared to the latter, that is, 1662 and 1171 $m^2\ g^{-1}$, respectively, possibly suggesting a more efficient removal of the organic part by means of H_3PO_4 rather than KOH, in line with the TG measurements [46,47]. Although the two samples have the same micro-pore volume (V_{mi}), approaching 0.6 $cm^3\ g^{-1}$, and an overall-pore volume (V_T) only slightly higher for AC-K compared to AC-H, with values of about 1.1 and 1.0 $cm^3\ g^{-1}$, respectively, the DFT plots of Fig. 2b show appreciable differences in pore size. Indeed, AC-K has pores with an average size below 0.8 nm, instead AC-H pores range around 1.5 nm. The analysis of the Hg porosimetry data reported in Fig. 2c shows relevantly different distribution of macro- and meso-pores (see table 4). AC-H has meso-pores with a volume (V_{me}) of about 0.4 $cm^3\ g^{-1}$, and a much lower macro-pores volume (i.e., V_{ma} of about 0.08 $cm^3\ g^{-1}$) compared to AC-K which contains predominantly macro-pores (V_{ma} = 0.5 $cm^3\ g^{-1}$). Furthermore, AC-K shows a slightly higher overall porosity compared to AC-H, that is, 1.13 and 0.97 $cm^3\ g^{-1}$,

respectively (V_T in Table 4). These remarkable differences indicate an actual effect of the activation conditions on the samples characteristics, and suggest a careful selection of the operating conditions adopted during the synthesis for achieving the appropriate properties.

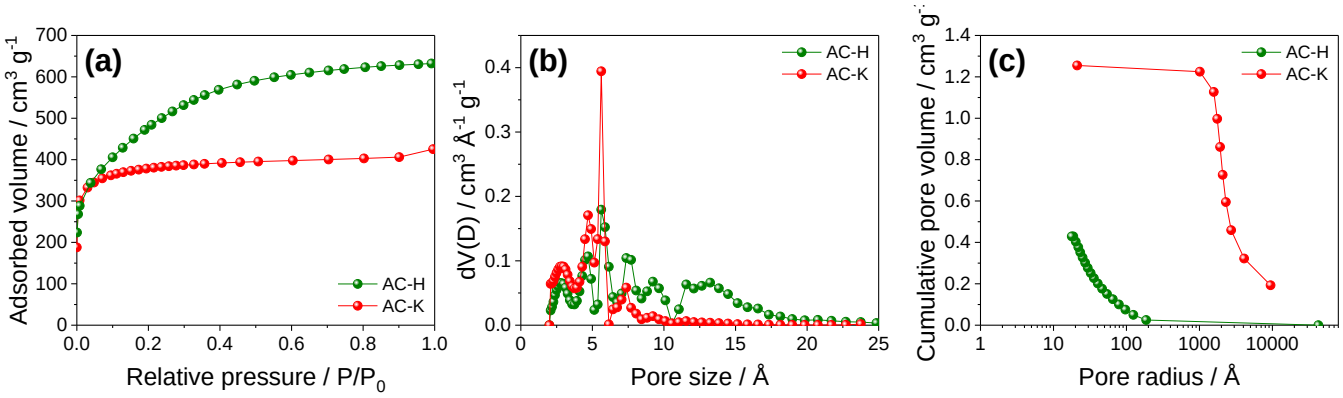

Figure 2. (a) N_2 adsorption BET isotherms recorded at 77 K, **(b)** pore size distribution obtained by density functional theory (DFT), and **(c)** cumulative pore volume trending determined by Hg porosimetry of AC-K (red) and AC-H (green) samples. See experimental section for sample's acronym.

Table 4. Surface area (S_{BET}), and micro-pores volume (V_{mi}) of AC-K, and AC-H as determined by N_2 adsorption-desorption BET isotherms. Volume of meso-pores (V_{me}), and macro-pores (V_{ma}) of AC-K, and AC-H as determined by Hg-porosimetry. V_T represents the overall sample porosity. See experimental section for sample's acronym.

Sample	S_{BET} ($m^2\ g^{-1}$)	V_{mi} (N_2) ($cm^3\ g^{-1}$)	V_{me} (Hg) ($cm^3\ g^{-1}$)	V_{ma} (Hg) ($cm^3\ g^{-1}$)	V_T (Hg) ($cm^3\ g^{-1}$)
AC-K	1171	0.57	0.08	0.48	1.13
AC-H	1662	0.57	0.40	0.08	0.97

Several literature papers have indicated the role of combination of the macro-, meso- and micro pores in enhancing the electrode performances in terms of *i)* electrolyte accessibility, and electrode wettability, which are particularly promoted by the macro and meso-pores [19], *ii)* ion diffusion

rate, and iii) charge transport kinetics at the electrode/electrolyte interphase which is mainly ascribed to micro pores [56]. Accordingly, a promoted electrolyte accessibility limits the cell polarization, thus favoring the energy efficiency, while low charge-transfer resistance, and fast ion diffusion at the electrode/electrolyte interphase favor the rate capability of the porous carbon materials [57]. Therefore, the simultaneous presence of various types of porosity into the hierarchical carbon actually allows enhanced performances of the electrode in energy storage devices [56].

The morphological characteristics of the samples are delighted by SEM, and TEM as reported in Figure 3. The samples reveal primary micrometric particles with bigger size for AC-K (about 200 μm, SEM in Fig. 3b) compared to AC-H (about 60 μm, Fig. 3d), likely due to the different activation pathway, as well as secondary particles with a size of about 20 μm (SEM insets in Fig. 3b and Fig. 3d). Flakes having submicron dimensions are also observed by the TEM images (Fig. 3a, c), mostly due to exfoliation of the carbon during the synthesis. Furthermore, the uniform presence of P into the AC-H sample, not detected by elemental analysis in Table 2, is herein confirmed by EDS mapping as reported in inset of Fig. 3d.

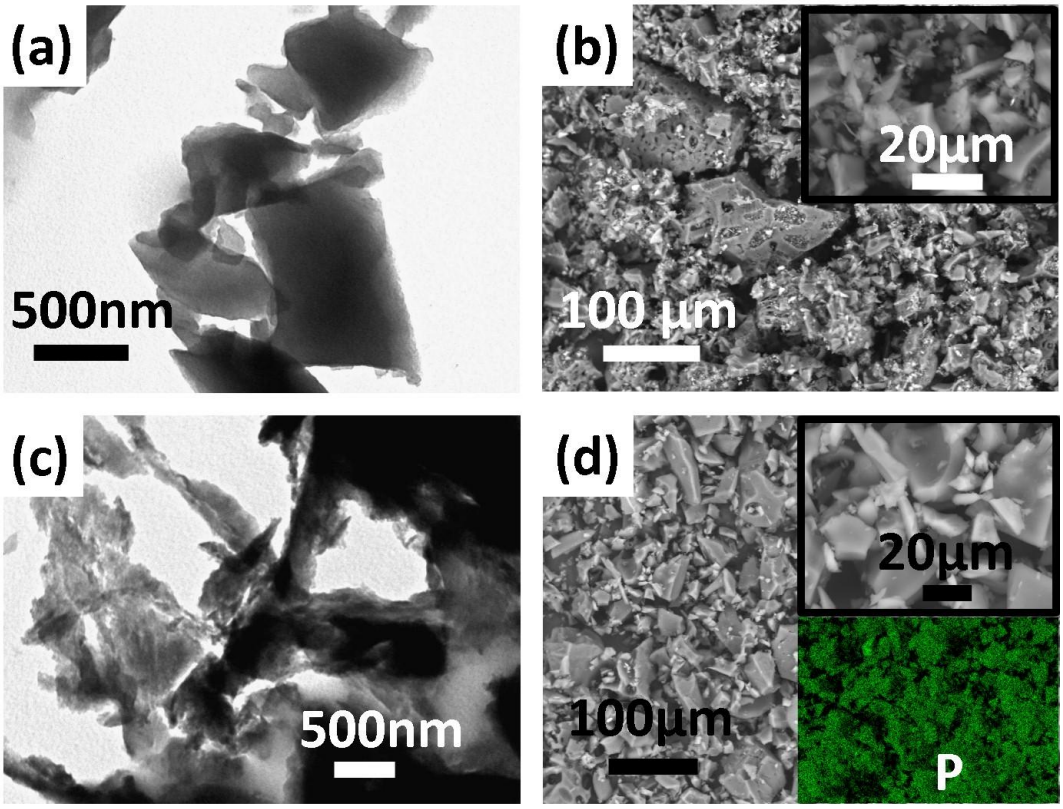

Figure 3. (**a**-**d**) Morphological study of the samples. (**a**, **c**) Transmission Electron Micrographs (TEM), (**b**, **d**) Scanning Electron Micrographs (SEM) of AC-K and AC-H, respectively. EDS mapping of P in AC-H sample is shown in the inset of Fig. 3d. See experimental section for sample's acronym.

The carbon electrodes are subsequently studied in lithium cell by combining voltammetry, impedance spectroscopy and galvanostatic measurements. Fig. 4a, and Fig. 4c show respectively the CV scans of AC-K, and AC-H electrodes in a three-electrode lithium cell between 0.01 and 2.8 V at a rate of 0.1 mV s^{-1}. Both samples show during the first cathodic scan a voltammetry profile significantly differing from the subsequent, characterized by a substantial irreversibility. Indeed, AC-K evidences only a broad signal extending below 1.0 V vs. Li^+/Li (inset of Fig. 4a), while the AC-H shows a first reduction peak at about 1.2 V, a small signal at about 0.7 V followed by a tilted line extending to 0.01 vs. Li^+/Li (inset of Fig. 4c). The differences between the curves related to AC-H and AC-K is particularly evidenced by the presence during the first cathodic scan of a peak at

the higher voltage value, i.e., 1.2 V vs. Li^+/Li, in the former and its absence in the latter. This discrepancy may be likely ascribed to the different nature, and extent of the impurities in the two electrodes. The elemental analysis of Table 2 actually reveals that AC-H contains about 6% of additional impurity compared to AC-K, which has been detected as P in the inset of the revised version of Fig. 3d. This impurity may possibly justify the side irreversible peak in the voltammetry curve related to AC-H. The irreversible trend of the first reduction is a typical characteristic of the electrochemical process in the carbons due to partial decomposition of the electrolyte, and the formation of a solid electrolyte interphase (SEI) layer at the electrode/electrolyte interphase [58,59]. The CV data also suggest additional irreversible processes ascribed to the specific impurities in the two carbon (revealed by TG and EDS): hence, AC-K mostly has organic residues while AC-H contains mainly an inorganic fraction constituted by phosphates [30]. The subsequent CV cycles are characterized by reversible, progressively overlapping profiles, with broad signals around 1.0 V, 0.2 V and 0.01 V vs. Li^+/Li due to the insertion/de-insertion of the lithium into the disordered carbon as well as to possible lithium plating/stripping into the pores of the active materials [60]. The achieved reversibility upon the first CV cycles likely indicates the stability of the SEI formed by the above mentioned irreversible reduction of the electrolyte [58–60], and of the residues detected in the activated carbons [38,61]. Additional insight on the electrode/electrolyte interphase characteristics are given by EIS analyses at the open-circuit voltage (OCV) and upon CV of the lithium cells using AC-K (Fig. 4b), and AC-H (Fig. 4d). Beside the electrolyte resistance, represented by the high-frequency intercept, the Nyquist plots show a middle-high frequency semicircle or deeply convoluted semicircles, accounting for both charge transfer and SEI film contributions in the electrode/electrolyte interphase, and a low-frequency tilted line with a slope approaching 45° likely related to the Warburg-type semi-infinite diffusion in the electrode or to cell geometric capacity [62–64]. Table 5 reports the values of the electrode/electrolyte interphase resistance, and the chi-square (χ^2) values obtained by nonlinear least squares (NLLS) method using a Boukamp tool [65], by adopting the equivalent circuits $R_e(R_iQ_i)Q_g$, where (R_iQ_i) are the resistances and the constant-

phase elements of the middle-high frequency semicircles ascribed to the interphase, R_e the electrolyte resistance, and Q_g the constant phase element related to the low-frequency line [66]. The accuracy of the data obtained by the analysis, evidenced by χ^2 values of about 10^{-4} or below, is achieved by adopting either one or two RQ elements, that is, $R_e(R_1Q_1)Q_g$ or $R_e(R_1Q_1)(R_2Q_2)Q_g$ for the analysis of the middle-high frequency semicircle of the interphase for AC-K, and AC-H electrodes, respectively. This discrepancy may be partially justified by a SEI film, and charge transfer processes having significantly different time-constant in AC-K and AC-H electrode/electrolyte interphase, leading to elements overlapping in one only in the latter, and to two distinguishable elements in the former [65,67]. Interestingly, Table 5 evidences that the first element vanishes by the ongoing of the voltammetry of the Li-cell using AC-K, with resistance value decreasing from about 7 Ω at the OCV to 1 Ω after 10 CV cycles.

Further difference between AC-K and AC-H interphases can be observed by taking into account the overall interphase resistance (R) reported in Table 5, and plotted in the inset of the corresponding Nyquist plot of Fig. 4b, and Fig. 4d, respectively. The figure reveals higher resistance for AC-K compared to AC-H with values of about 33 Ω and 3 Ω, respectively, at the OCV. After 1 CV cycle, the resistance decreases to about 21 Ω for AC-K, while it raises to about 24 Ω for AC-H, to finally increase after 5 and 10 CV cycles to 43 Ω, and 78 Ω for AC-K, and to 32 Ω, and 40 Ω for AC-H, respectively. These trends as well as the different CV responses may be likely ascribed to the nature of each carbon in terms of composition, and morphology which may actually influence the electrochemical behavior of the electrode, and of possible side reaction [68,69].

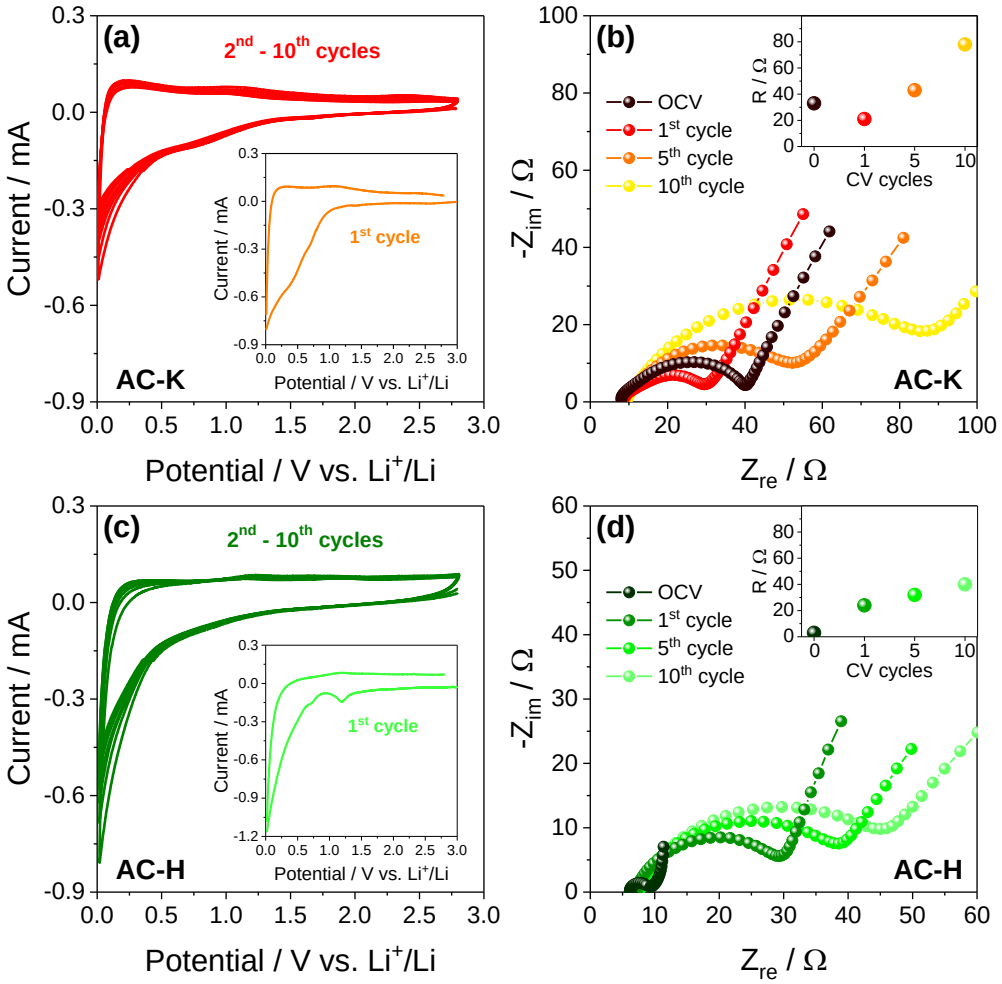

Figure 4. (**a-d**) Electrochemical features of the electrodes and characteristics of the electrode/electrolyte interphase. (**a**, **c**) Cyclic voltammetry profiles (CV) of (**a**) AC-K and (**c**) AC-H in three-electrode T-cell using lithium as counter and reference electrodes at a scan rate of 0.1 mV s^{-1}, from 0.01V to 2.8V, and (**b**, **d**) corresponding Nyquist plot of the Electrochemical Impedance Spectroscopy (EIS), respectively, at the OCV, after 1, 5 and 10 voltammetry cycles. Electrolyte: EC, DMC 1:1 (w/w), 1M $LiPF_6$. Alternate signal amplitude: 10 mV. Frequency range: 500 kHz - 100 mHz. Temperature: 25 °C. See experimental section for sample's acronym.

In this respect, it may be worth noting that the additional decomposition peak at about 1.2 V vs. Li/Li^+ observed for AC-H during the first cathodic scan (inset of Fig 4c) may actually lead to the initial increase of the interphase resistance observed in inset of Fig. 4d, while CV profile in AC-K (inset of Fig. 4a) can likely favor the SEI formation as suggested by the initial impedance decrease

in the corresponding trend in inset Fig. 4b. On the other hand, the subsequent CV cycles lead for both samples to an increase of the interphase resistance due to the SEI growth.

Table 5. Electrode/electrolyte interphase resistance and chi-square (χ^2) values obtained by NLLS analyses using a Boukamp tool of the impedance spectra of AC-K (Figure 3b), and AC-H (Figure 3d) in three-electrode T-cell using lithium as counter and reference electrodes at the OCV, after 1, 5 and 10 voltammetry cycles at a 0.1 mV s^{-1} scan rate within the potential range from 0.01 to 2.8 V vs Li^+/Li (reported in Figure 3a and Figure 3b, respectively). Electrolyte: EC, DMC 1:1 (w/w), 1M $LiPF_6$. Alternate signal amplitude: 10 mV. Frequency range: 500 kHz - 100 mHz. Temperature: 25 °C. See experimental section for sample's acronym.

AC-K					
Cell condition	Circuit	R_1 [Ω]	R_2 [Ω]	$R=R_1 + R_2$ [Ω]	χ^2
OCV	$R_e(R_1Q_1)(R_2Q_2)Q_g$	6.5 ± 1.4	26.6 ± 1.5	33.1± 2.9	4×10^{-5}
1 CV cycle	$R_e(R_1Q_1)(R_2Q_2)Q_g$	5.5 ± 0.7	15.8 ± 0.7	21.3 ± 1.4	2×10^{-5}
5 CV cycles	$R_e(R_1Q_1)(R_2Q_2)Q_g$	2.9 ± 0.7	39.6 ± 1.0	42.5 ± 1.7	4×10^{-5}
10 CV cycles	$R_e(R_1Q_1)(R_2Q_2)Q_g$	1.1 ± 0.3	76.5± 0.8	77.6 ± 1.1	4×10^{-5}
AC-H					
OCV	$R_e(R_1Q_1)Q_g$	2.9 ± 0.1	-	2.88 ± 0.1	2×10^{-4}
1 CV cycle	$R_e(R_1Q_1)Q_g$	23.5 ± 0.2	-	23.5 ± 0.2	8×10^{-5}
5 CV cycles	$R_e(R_1Q_1)Q_g$	32.3 ± 0.4	-	32.3 ± 0.4	7×10^{-5}
10 CV cycles	$R_e(R_1Q_1)Q_g$	39.5 ± 0.6	-	39.5 ± 0.6	5×10^{-5}

Hence, the characteristic electrode/electrolyte interphases in AC-K and AC-H is expected to influence the electrochemical response of the two materials both in lithium half-cell, and in lithium-ion full cell. Therefore, the applicability of the two electrodes is investigated in lithium cell galvanostatically cycled at different currents by adopting various protocols. Indeed, Figure 5 reports the cycling responses of AC-K (red curves), and AC-H (green curves) in lithium cell at a C/3 rate, and their rate capability at C/10, C/5, C/3, C/2, 1C, 2C and 5C (1C = 372 mA g^{-1}). Both AC-H and AC-K show during the initial 20 cycles a capacity decreasing from about 330 mAh g^{-1} to about 200 mAh g^{-1} (Fig. 5a). This trend, likely expected by progressive decomposition of the impurities in the two carbons, is reflected by the voltage profiles (Fig. 5c and Fig. 5e, respectively) which

significantly change from the 1st cycle (insets of the figures), to the 2nd, the 10th, and to the 20th cycle. Subsequently, the voltage trends of Fig. 5c and Fig. 4e reflect for both materials the typical sloping shape ascribed to the insertion of lithium into the disordered carbon below 1.2 V [68]. The above side processes initially depress the delivered capacity, and decrease the coulombic efficiency, which has a value below 50% during the first cycle (Fig. 5a); however, the processes leads also to the formation of a very stable interphase during the subsequent cycles [27] with an efficiency approaching 100%, and a reversible trend. This relevant stability is well justified by the inset of Fig. 5a which shows the trends of the electrode/electrolyte interphase resistance of the lithium half-cells using AC-K (red), and AC-H (green) upon the galvanostatic cycling at C/3 (see Figure S1 and Table S1 in the Supplementary Material for the corresponding Nyquist plots, and NLLS analyses). The data reveal a remarkable decrease of the overall electrode/electrolyte resistance for the cells, including both lithium anode, and either AC-K or AC-H, from about 48 Ω and 18 Ω, respectively, to low and constant values ranging between 7 and 9 Ω, thus further accounting for the electrode suitability for prolonged cycling. Hence, AC-H reveals a decrease of the specific capacity from about 200 at the 20th cycle to about 170 mAh g^{-1} upon 200 cycles, while AC-K shows a capacity slightly increasing, i.e., from 200 to about 210 mAh g^{-1}, upon the same number of cycles (Fig. 4a). The rate capability of the two samples in lithium cell is examined at the current of C/10, C/5, C/3, C/2, 1C, 2C and 5C (1C = 372 mA g^{-1}), and reported in terms of cycling trend (Fig. 5b), and voltage profile of selected cycles (Fig. 5d and Fig. 5f for AC-K and AC-H, respectively). The two samples evidence the initial decay already discussed above, and a different rate capability, with a higher delivered capacity for AC-H compared to AC-K at currents lower than C/2; accordingly, AC-H has an average capacity ranging from about 400 mAh g^{-1} at C/10 to 230 mAh g^{-1} at C/3, while AC-K shows an average value from about 320 mAh g^{-1} at C/10 to 200 mAh g^{-1} at C/3. This trend is reversed at C-rates higher than C/2, with an average capacity of AC-H ranging from about 120 mAh g^{-1} at 1C to 40 mAh g^{-1} at 5C for AC-H, and a value from about 140 mAh g^{-1} at 1C to 70 mAh g^{-1} at 5C for AC-K. The lower value of the capacity obtained at the higher currents is likely

attributed to the increase of the cell polarization, as evidenced by the voltage profiles of the rate capability tests reported in Fig. 5d and Fig. 5f for AC-K and AC-H, respectively. It is worth mentioning that the capacity values of AC-H, estimated by considering the carbon content only, i.e., by excluding 15 % of impurity observed above (see discussion of Fig. 1), may be actually higher than the ones observed in Fig. 5, thus further accounting for the differences observed between the two samples. Therefore, the difference observed between the two samples in terms of reversible capacity, and value of the electrode/electrolyte interphase resistance (Table 5) may be actually driven by the different nature of impurities, the textural properties, a greater BET surface of AC-H compared to the AC-K, the significant mesopore content interconnected with the micropores in AC-H, and the predominant presence of macroporous in with AC-K sample.

In overall, the galvanostatic tests in half-cell evidence the applicability of the two materials as the anode in Li-ion cell. However, the data of Fig. 5 suggest a preliminary treatment of the electrodes before use in full-cell in order to avoid the detrimental effect of the initial capacity decay, and achieve a suitable reversibility for an efficient application. In this respect, several procedures have been proposed, in particular for amorphous carbons and Li-alloy electrodes characterized by relevant irreversible capacity during the initial cycles [70–72]. Among them, electrochemical activation by pre-cycling of the electrodes in lithium half-cell [72], via surface modification and coatings [73], or by direct contact with lithium metal [70,71] evidenced the most suitable results in terms of stability of the full-cell. Therefore, prior to use AC-K and AC-H in full cell exploiting $LiFePO_4$ olivine-structure cathode [74] the two electrodes are electrochemically activated in half-cell by 30 galvanostatic cycles at C/3 to achieve the steady state observed in Fig. 5 (see experimental section for further details). The cells are balanced by slight anode excess with an N/P capacity ratio of about 1.03, according to the mass loading reported in the experimental section, considering the theoretical capacity of 170 mAh g^{-1} for $LiFePO_4$ (see corresponding cycling in half cell in Figure S2 in Supplementary Material) and a practical capacity at the steady state of about 200 mAh g^{-1} for the carbon electrodes.

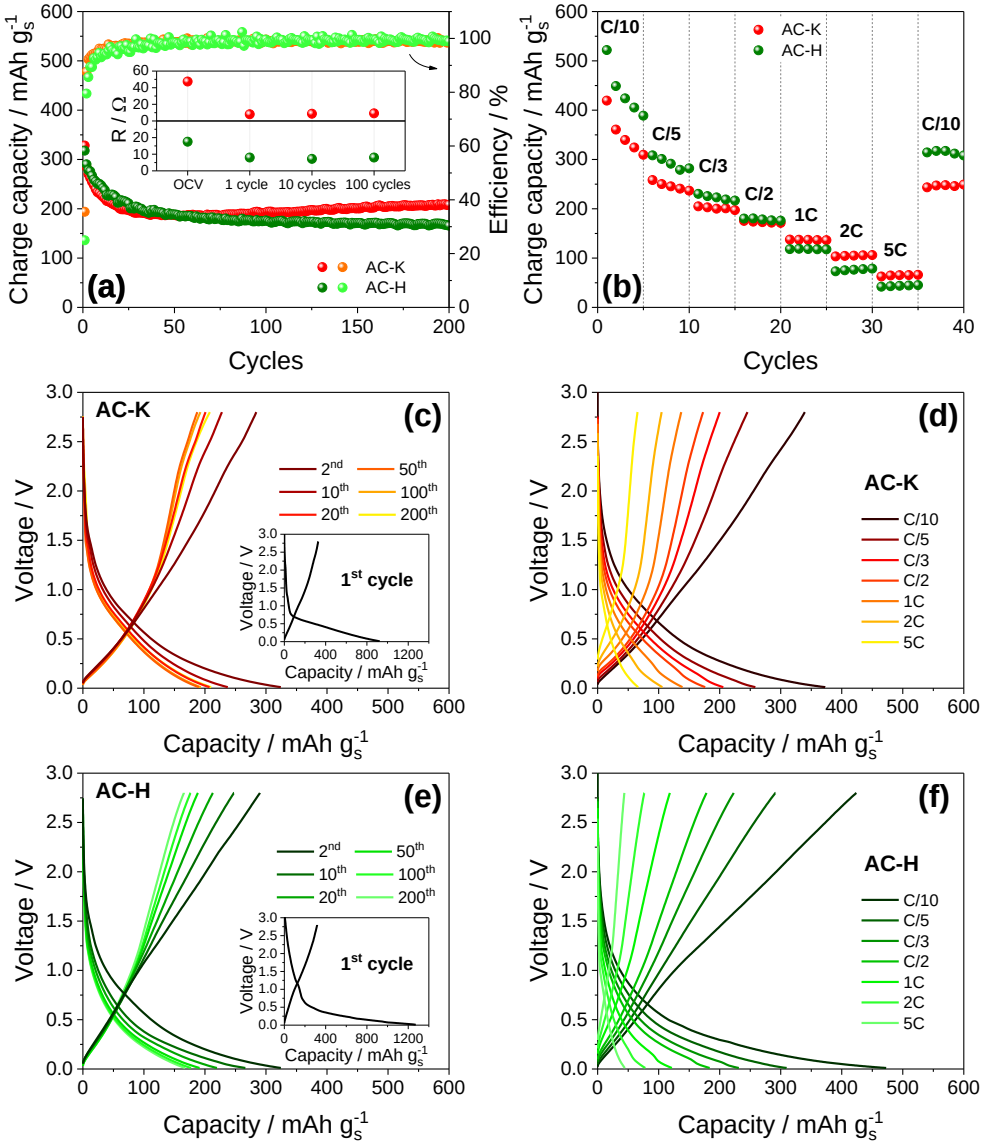

Figure 5. **(a-f)** Cycling performances of the electrodes in lithium half-cell. (**a**) Cycling trend with coulombic efficiency (right Y axis) of AC-K (red), and AC-H (green) in a lithium cell galvanostatically cycled at a C/3 rate (1C = 372 mA g^{-1}), and (**c**, **e**) corresponding voltage profiles, respectively, for selected cycles; inset in panel (a) shows the electrode/electrolyte interphase resistance values of the AC-K (red), and AC-H (green) measured by EIS upon the cycling at C/3 (see Figure S1 and Table S1 in the Supplementary Material for the corresponding Nyquist plots and NLLS analyses). (**b**) Rate capability cycling trend of AC-K (red), and AC-H (green) in a lithium cell galvanostatically cycled at C/10, C/5, C/3, C/2, 1C, 2C and 5C, and (**d**, **f**) corresponding voltage profiles, respectively, of selected cycles. Electrolyte: EC, DMC 1:1 (w/w), 1M $LiPF_6$. Voltage limits: 0.01-2.8 V. Temperature: 25 °C. See experimental section for sample's acronym.

Figure 6 reports the cycling performances of AC-K (red), and AC-H (green) in the lithium-ion full-cell, both at the constant c-rate of C/3 (1C = 170 mA g^{-1}) for evaluating the cycle life (Fig. 6a), and at various c-rates to determine the rate capability (Fig. 6b). After the initial few cycles characterized by some side irreversible processes dealing with electrolyte oxidation at the higher voltages, and possible reduction at the lower voltage values [75], the two cells remarkably deliver a steady state capacity of about 160 mAh g^{-1}, that is, a value of about 95% of the theoretical value of $LiFePO_4$. The corresponding voltage profiles, reported in Fig. 6c for AC-K, and Fig. 6e for AC-H, clearly evidence during the initial cycles the above mentioned processes likely occurring at about 3.6 V during charge and at 0.6 V during discharge. Furthermore, the steady state charge/discharge profile reflects the combination between the flat profile typical of the insertion process of the $LiFePO_4$ occurring at about 3.5 V vs. Li^+/Li [74], and the sloping one extending from about below 1.5 V until low potential of AC-K, and AC-H (compare with Fig. 5c, and Fig. 5e, respectively). Therefore, the cells show at the steady state a capacity approaching 160 mAh g^{-1} delivered with an average working voltage of about 2.8 V, thus a theoretical energy density of about 450 Wh kg^{-1} [1]. Remarkably, both cells evidence high efficiency after the initial cycles, and a relevant stability by the subsequent cycles (Fig. 6a). Hence, the cell using AC-K reveals a coulombic efficiency of about 98% (upon 20 cycles) leading to a capacity retention of 94% with respect to the steady state (160 mAh g^{-1}) upon 200 cycles, while the cell using AC-H shows after 20 cycles a coulombic efficiency higher than 99%, and a capacity retention as high as 96%. It is worth mentioning that the voltage shape of the cells (Fig. 6c for AC-K and Fig. 6e for AC-H) progressively modifies during cycles, in particular during the final stages of the test, likely due to a slight change of the cell balance promoted by the side processes, however without significant change of the delivered capacity [72]. The rate capability of the two full-cells is examined at currents increasing from C/5 to C/3, 1C and 2C (Fig. 6b). After the initial cycles at C/5 during which the cells undergo side reactions affecting the delivered capacity, the figure shows stable values of about 162, 159, 123, and 79 mAh g^{-1} for

the cell using AC-K, and 156, 148, 98, and 67 mAh g^{-1} for the cell using AC- H at C/5, C/3, 1C and 2C, respectively.

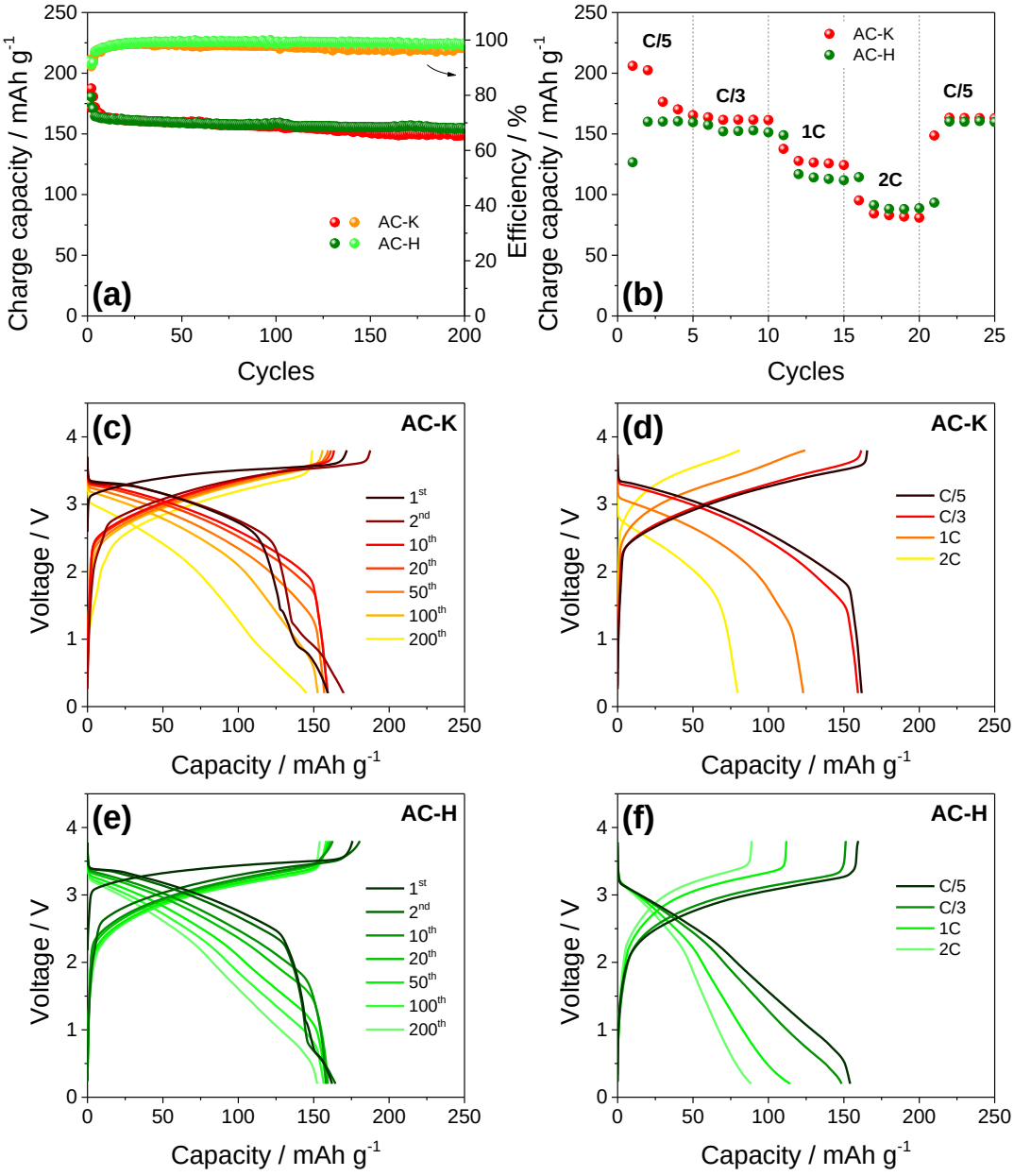

Figure 6. **(a-f)** Cycling performances of the electrodes in lithium-ion full-cell using a $LiFePO_4$ cathode. (**a**) Cycling trend with coulombic efficiency (right Y axis) of AC-K (red), and AC-H (green) in a lithium-ion cell galvanostatically cycled at a C/3 rate (1C = 170 mA g^{-1}), and (**c**, **e**) corresponding voltage profiles, respectively, for selected cycles. (**b**) Rate capability cycling trend of AC-K (red), and AC-H (green) in a lithium-ion cell galvanostatically cycled at C/5, C/3, 1C, and 2C, and (**d**, **f**) corresponding voltage profiles, respectively, of selected cycles. Electrolyte: EC,

DMC 1:1 (w/w), 1M $LiPF_6$. Voltage limits: 0.2-3.8 V. Temperature: 25 °C. See experimental section for sample's acronym.

Therefore, the cells show the expected decrease of the delivered capacity by raising the current due to the increase of the polarization (Fig. 6d, and Fig. 6f for AC-K, and AC-H, respectively), however with an excellent rate capability. Compared to the half-cells, the full cells using the two carbons reveal less differences, most likely due to the pre-activation process prior to cycling which mitigates the irreversible processes ascribed to the different samples' nature, and composition. Despite further insights may be required to fully setup the activation pathway of AC-K and AC-H for achieving a low impurity content, the remarkable performances of the lithium-ion cells reported above actually suggest the two electrodes as alternative anode materials for a safe, low cost, and environmentally sustainable energy storage.

4. Conclusions

Several literature papers reported carbons derived from bio masses for application as anode in lithium battery. Among them, loofah-derived pseudo-graphite (LPG) prepared through alkali treatment process followed by pyrolysis was used in Li-cell with specific capacity of 225 mAh g^{-1} after 200 cycles at the current density of 100 mA g^{-1} [25]. A carbonaceous material obtained by mechanochemical dry milling of spent coffee grounds (SCG), and carbonization at 800 C delivered in lithium cell initial specific capacity of 360 mAh g^{-1} current density of 0.1 A g^{-1}, and a reversible capacity of 285 mAh g^{-1} over 100 cycles [26]. Honey derived mesoporous nitrogen-doped carbons (HMNCs) showed a reversible capacity of about 700 mA h g^{-1} after 200 cycles at 1 A g^{-1} [27], while carbon nanofibers (CNFs) prepared by liquefying the biomass, electrospinning and carbonizing at high temperature exhibited a specific capacity of 272 mA h g^{-1} at 30 mA g^{-1}, good rate capability (131 and 102 mA h g^{-1} at 1 A g^{-1} and 2 A g^{-1}, respectively), and excellent cycling performance [28]. Disordered carbons obtained from cherry stones were tested as electrodes for lithium batteries up to 100 cycles from C/10 to 5C, with specific capacity of 200 mAh g^{-1} at 5C

[29]. Microtubular carbons obtained from bamboo and woods by acid treatment, and carbonization were used in lithium battery with capacity of 435 mA h g^{-1} at 50 mA g^{-1}, 150 mA h g^{-1} at 2 A g^{-1}, and 76% capacity retention at 500 mA g^{-1} upon 500 cycles [30]. Hard carbon from a natural gel derived from the Basil seeds (*Osimum Basilicum*) obtained by pyrolysis of the freeze- dried mucilage possesses sheet- like, showed a reversible capacity of 195 mAh g^{-1} at 0.1 A g^{-1} with 91 % retention after 300 cycles [31]. Three-dimensional (3D) rod-like carbon micro-structures derived from natural ramie fibers, and two-dimensional (2D) carbon nanosheets derived from corncobs prepared by heat treatment exhibited a capacity of 489 and 606 $mAhg^{-1}$ after 180 cycles at current density of 100 mAg^{-1} [32]. However, the good performances in terms of delivered capacity, cycle life and rate capability for large part of the above carbons were principally obtained in lithium half-cell rather than Li-ion full cell.

In our work, two carbon materials derived from cherry pit, and differing by the activation pathway have been fully characterized for application as the anode in Li-ion battery. The two materials revealed slightly different structure and morphology and, in particular, a different content and nature of the impurity depending on the adopted activation method. Indeed, the material treated by KOH (indicated by AC-K) revealed more relevant organic fraction, while the material activated by H_3PO_4 (indicated by AC-H) mostly showed an inorganic residual. The two samples have also shown significant differences of textural properties. AC-H sample evidenced a BET surface higher by 40% compared to AC-K, and a micro-/mesopore system rather than micro-/macropore one. These differences have been reflected into a characteristic electrochemical behavior in lithium cell, both in terms of the voltage shape, the rate capability, and of the delivered capacity. However, upon the initial irreversible cycles due to the above mentioned impurities, the two materials revealed very stable and reversible trends, whit steady state capacity approaching 200 mAh $g^{-1,}$ which suggested the applicability in lithium-ion full cell upon an electrochemical pre-treatment. Therefore, electrochemically pre-cycled AC-K and AC-H electrodes have been used in a full cell in combination with a $LiFePO_4$ electrode. The Li-ion cells delivered a very stable capacity

approaching the theoretical value of the cathode with a cycle life extended over 200 cycles, an efficiency approaching 100% upon the initial stage, a retention exceeding 90%, and a rate capability extending over 2C. Considering a cell capacity of 160 mAh g^{-1} and an average working voltage of about 2.8 V, the two cells delivered a theoretical energy density of about 450 Wh kg^{-1}, which may be actually reflected into a practical value exceeding 150 Wh kg^{-1}. These performances suggested the AC-K and AC-H materials as anodes for application in efficient Li-ion cell characterized by a remarkable stability, and a relevant environmental sustainability. However, the results also indicated that further work is needed in order to optimize the synthesis procedure to achieve high-purity carbons, and limit the effects of the side reactions during cell cycling.

Acknowledgements

This work was funded by the grant "Fondo per l'Incentivazione alla Ricerca (FIR) 2018", University of Ferrara, and performed within the collaboration project "Accordo di Collaborazione Quadro 2015" between University of Ferrara (Department of Chemical and Pharmaceutical Sciences) and Sapienza University of Rome (Department of Chemistry). Likewise, this research was funded by Ministerio de Economía y Competitividad (Project MAT2017-87541-R) and Junta de Andalucía (Group FQM-175).

References

[1] D. Di Lecce, R. Verrelli, J. Hassoun, Lithium-ion batteries for sustainable energy storage: Recent advances towards new cell configurations, Green Chem. 19 (2017) 3442–3467. doi:10.1039/c7gc01328k.

[2] C. McGlade, P. Ekins, The geographical distribution of fossil fuels unused when limiting global warming to 2 °C, Nature. 517 (2015) 187–190. doi:10.1038/nature14016.

[3] C.D. Thomas, A. Cameron, R.E. Green, M. Bakkenes, L.J. Beaumont, Y.C. Collingham, et al., Extinction risk from climate change, Nature. 427 (2004) 145–148.

doi:10.1038/nature02121.

[4] J. Xu, S. Dou, H. Liu, L. Dai, Cathode materials for next generation lithium ion batteries, Nano Energy. 2 (2013) 439–442. doi:10.1016/j.nanoen.2013.05.013.

[5] R. Van Noorden, The rechargeable revolution: A better battery, Nature. 507 (2014) 26–28. doi:10.1038/507026a.

[6] J. Xu, Y. Dou, Z. Wei, J. Ma, Y. Deng, Y. Li, et al., Recent Progress in Graphite Intercalation Compounds for Rechargeable Metal (Li, Na, K, Al)-Ion Batteries, Adv. Sci. 4 (2017). doi:10.1002/advs.201700146.

[7] M. Ashuri, Q. He, L.L. Shaw, Silicon as a potential anode material for Li-ion batteries: where size, geometry and structure matter, Nanoscale. 8 (2016) 74–103. doi:10.1039/C5NR05116A.

[8] A.R. Kamali, D.J. Fray, Tin-based materials as advanced anode materials for lithium ion batteries: A review, Rev. Adv. Mater. Sci. 27 (2011) 14–24.

[9] J. Hassoun, P. Ochal, S. Panero, G. Mulas, C. Bonatto Minella, B. Scrosati, The effect of CoSn/CoSn2 phase ratio on the electrochemical behaviour of Sn40Co40C20 ternary alloy electrodes in lithium cells, J. Power Sources. 180 (2008). doi:10.1016/j.jpowsour.2008.01.059.

[10] G.A. Elia, U. Ulissi, S. Jeong, S. Passerini, J. Hassoun, Exceptional long-life performance of lithium-ion batteries using ionic liquid-based electrolytes, Energy Environ. Sci. 9 (2016) 3210–3220. doi:10.1039/c6ee01295g.

[11] H.-G. Jung, M.W. Jang, J. Hassoun, Y.-K. Sun, B. Scrosati, A high-rate long-life Li4Ti5O12/Li[Ni0.45Co0.1Mn1.45]O4 lithium-ion battery, Nat. Commun. 2 (2011) 516. doi:10.1038/ncomms1527.

[12] T. Tsumura, A. Katanosaka, I. Souma, T. Ono, Y. Aihara, J. Kuratomi, et al., Surface modification of natural graphite particles for lithium ion batteries, Solid State Ionics. 135 (2000) 209–212. doi:10.1016/S0167-2738(00)00365-9.

[13] O.A. Vargas C., Á. Caballero, J. Morales, Can the performance of graphene nanosheets for lithium storage in Li-ion batteries be predicted?, Nanoscale. 4 (2012) 2083. doi:10.1039/c2nr11936f.

[14] R. Verrelli, J. Hassoun, High capacity tin–iron oxide-carbon nanostructured anode for advanced lithium ion battery, J. Power Sources. 299 (2015) 611–616. doi:10.1016/j.jpowsour.2015.09.034.

[15] R. Verrelli, J. Hassoun, High-Capacity NiO-(Mesocarbon Microbeads) Conversion Anode for Lithium-Ion Battery, ChemElectroChem. 2 (2015) 988–994. doi:10.1002/celc.201500069.

[16] C. Hernández-Rentero, O. Vargas, A. Caballero, J. Morales, F. Martín, Solvothermal-induced 3D graphene networks: Role played by the structural and textural properties on lithium storage, Electrochim. Acta. 222 (2016) 914–920. doi:10.1016/j.electacta.2016.11.057.

[17] R. Mo, F. Li, X. Tan, P. Xu, R. Tao, G. Shen, et al., High-quality mesoporous graphene particles as high-energy and fast-charging anodes for lithium-ion batteries, Nat. Commun. 10 (2019) 1–10. doi:10.1038/s41467-019-09274-y.

[18] D. Di Lecce, P. Andreotti, M. Boni, G. Gasparro, G. Rizzati, J.-Y. Hwang, et al., Multiwalled Carbon Nanotubes Anode in Lithium-Ion Battery with LiCoO 2 , Li[Ni 1/3 Co 1/3 Mn 1/3]O 2 , and LiFe 1/4 Mn 1/2 Co 1/4 PO 4 Cathodes, ACS Sustain. Chem. Eng. 6 (2018) 3225–3232. doi:10.1021/acssuschemeng.7b03395.

[19] L. Wang, X. Hu, Recent Advances in Porous Carbon Materials for Electrochemical Energy

Storage, Chem. - An Asian J. 13 (2018) 1518–1529. doi:10.1002/asia.201800553.

[20] J. Chen, C. Li, Z. Ristovski, A. Milic, Y. Gu, M.S. Islam, et al., A review of biomass burning: Emissions and impacts on air quality, health and climate in China, Sci. Total Environ. 579 (2017) 1000–1034. doi:10.1016/j.scitotenv.2016.11.025.

[21] L. Jiang, L. Sheng, Z. Fan, Biomass-derived carbon materials with structural diversities and their applications in energy storage, Sci. China Mater. 61 (2018) 133–158. doi:10.1007/s40843-017-9169-4.

[22] J. Jiang, K. Zhu, Y. Fang, H. Wang, K. Ye, J. Yan, et al., Coralloidal carbon-encapsulated CoP nanoparticles generated on biomass carbon as a high-rate and stable electrode material for lithium-ion batteries, J. Colloid Interface Sci. 530 (2018) 579–585. doi:10.1016/j.jcis.2018.07.019.

[23] C. Chen, Y. Huang, Y. Zhu, Z. Zhang, Z. Guang, Z. Meng, et al., Nonignorable Influence of Oxygen in Hard Carbon for Sodium Ion Storage, ACS Sustain. Chem. Eng. 8 (2020) 1497–1506. doi:10.1021/acssuschemeng.9b05948.

[24] P. Sennu, N. Arun, S. Madhavi, V. Aravindan, Y.-S. Lee, All carbon based high energy lithium-ion capacitors from biomass: The role of crystallinity, J. Power Sources. 414 (2019) 96–102. doi:10.1016/j.jpowsour.2018.12.089.

[25] Z. Wu, L. Wang, J. Huang, J. Zou, S. Chen, H. Cheng, et al., Loofah-derived carbon as an anode material for potassium ion and lithium ion batteries, Electrochim. Acta. 306 (2019) 446–453. doi:10.1016/j.electacta.2019.03.165.

[26] F. Luna-Lama, D. Rodríguez-Padrón, A.R. Puente-Santiago, M.J. Muñoz-Batista, A. Caballero, A.M. Balu, et al., Non-porous carbonaceous materials derived from coffee waste grounds as highly sustainable anodes for lithium-ion batteries, J. Clean. Prod. 207 (2019) 411–417. doi:10.1016/j.jclepro.2018.10.024.

[27] Y. Zhang, L. Chen, Y. Meng, J. Xie, Y. Guo, D. Xiao, Lithium and sodium storage in highly ordered mesoporous nitrogen-doped carbons derived from honey, J. Power Sources. 335 (2016) 20–30. doi:10.1016/j.jpowsour.2016.08.096.

[28] L. Tao, Y. Huang, X. Yang, Y. Zheng, C. Liu, M. Di, et al., Flexible anode materials for lithium-ion batteries derived from waste biomass-based carbon nanofibers: I. Effect of carbonization temperature, RSC Adv. 8 (2018) 7102–7109. doi:10.1039/c7ra13639k.

[29] J.C. Arrebola, A. Caballero, L. Hernán, J. Morales, V. Gómez-Serrano, Improving the Performance of Biomass-Derived Carbons in Li-Ion Batteries by Controlling the Lithium Insertion Process, J. Electrochem. Soc. 157 (2010) A791–A797. doi:10.1149/1.3425728.

[30] X. Zhang, J. Hu, X. Chen, M. Zhang, Q. Huang, X. Du, et al., Microtubular carbon fibers derived from bamboo and wood as sustainable anodes for lithium and sodium ion batteries, J. Porous Mater. (2019). doi:10.1007/s10934-019-00781-3.

[31] N. Sharma, Y. Gawli, A. Ahmad, M. Muhammed, S. Ogale, Nanotubular Hard Carbon Derived from Renewable Natural Seed Gel for High Performance Sodium-Ion Battery Anode, ChemistrySelect. 2 (2017) 6909–6915. doi:10.1002/slct.201701123.

[32] Q. Jiang, Z. Zhang, S. Yin, Z. Guo, S. Wang, C. Feng, Biomass carbon micro/nano-structures derived from ramie fibers and corncobs as anode materials for lithium-ion and sodium-ion batteries, Appl. Surf. Sci. 379 (2016) 73–82. doi:10.1016/j.apsusc.2016.03.204.

[33] A.A. Arie, B. Tekin, E. Demir, R. Demir-Cakan, Hard carbons derived from waste tea bag powder as anodes for sodium ion battery, Mater. Technol. 34 (2019) 515–524. doi:10.1080/10667857.2019.1586087.

[34] N. Moreno, A. Caballero, L. Hernán, J. Morales, Lithium–sulfur batteries with activated carbons derived from olive stones, Carbon N. Y. 70 (2014) 241–248. doi:10.1016/j.carbon.2014.01.002.

[35] A. Benítez, M. González-Tejero, Á. Caballero, J. Morales, Almond shell as a microporous carbon source for sustainable cathodes in lithium-sulfur batteries, Materials (Basel). 11 (2018) 1428. doi:10.3390/ma11081428.

[36] H. Chen, P. Xia, W. Lei, Y. Pan, Y. Zou, Z. Ma, Preparation of activated carbon derived from biomass and its application in lithium–sulfur batteries, J. Porous Mater. 26 (2019) 1325–1333. doi:10.1007/s10934-019-00720-2.

[37] M. Shahbandeh, Cherry production worldwide from 2000 to 2017, 2019-02-01. (2019). https://www.statista.com/statistics/577489/world-cherry-production/.

[38] Z. Li, Z. Xu, X. Tan, H. Wang, C.M.B. Holt, T. Stephenson, et al., Mesoporous nitrogen-rich carbons derived from protein for ultra-high capacity battery anodes and supercapacitors, Energy Environ. Sci. 6 (2013) 871–878. doi:10.1039/c2ee23599d.

[39] K. Hong, L. Qie, R. Zeng, Z. Yi, W. Zhang, D. Wang, et al., Biomass derived hard carbon used as a high performance anode material for sodium ion batteries, J. Mater. Chem. A. 2 (2014) 12733. doi:10.1039/C4TA02068E.

[40] J. Wang, S. Kaskel, KOH activation of carbon-based materials for energy storage, J. Mater. Chem. 22 (2012) 23710–23725. doi:10.1039/c2jm34066f.

[41] M.S. Solum, R.J. Pugmire, M. Jagtoyen, F. Derbyshire, Evolution of carbon structure in chemically activated wood, Carbon N. Y. 33 (1995) 1247–1254. doi:10.1016/0008-6223(95)00067-N.

[42] H.J. Denisa, A.M. Puziy, O.I. Poddubnaya, S.G. Fabian, J.M.D. Tascón, G.Q. Lu, Highly stable performance of supercapacitors from phosphorus-enriched carbons, J. Am. Chem. Soc. 131 (2009) 5026–5027. doi:10.1021/ja809265m.

[43] C. Hernández-Rentero, R. Córdoba, N. Moreno, A. Caballero, J. Morales, M. Olivares-Marín, et al., Low-cost disordered carbons for Li/S batteries: A high-performance carbon

with dual porosity derived from cherry pits, Nano Res. 11 (2018) 89–100. doi:10.1007/s12274-017-1608-1.

[44] F. Croce, A. D' Epifanio, J. Hassoun, A. Deptula, T. Olczac, B. Scrosati, A Novel Concept for the Synthesis of an Improved LiFePO[sub 4] Lithium Battery Cathode, Electrochem. Solid-State Lett. 5 (2002) A47. doi:10.1149/1.1449302.

[45] S. Wei, Z. Li, K. Kimura, S. Inoue, L. Pandini, D. Di Lecce, et al., Glyme-based electrolytes for lithium metal batteries using insertion electrodes: An electrochemical study, Electrochim. Acta. 306 (2019) 85–95. doi:10.1016/j.electacta.2019.03.051.

[46] M. Olivares-Marin, C. Fernandez-Gonzalez, A. Macias-Garcia, V. Gomez-Serrano, Preparation of activated carbons from cherry stones by activation with potassium hydroxide, Appl. Surf. Sci. 252 (2006) 5980–5983. doi:10.1016/j.apsusc.2005.11.018.

[47] M. Olivares-Marin, C. Fernandez-Gonzalez, A. Macias-Garcia, V. Gomez-Serrano, Porous structure of activated carbon prepared from cherry stones by chemical activation with phosphoric acid, Energy and Fuels. 21 (2007) 2942–2949. doi:10.1021/ef060652u.

[48] S. Brutti, J. Hassoun, B. Scrosati, C. Lin, H. Wu, H. Hsieh, A high power Sn-C/C-LiFePO4 lithium ion battery, J. Power Sources. 217 (2012) 72–76. doi:10.1016/j.jpowsour.2012.05.102.

[49] M.M. DUBININ, Physical Adsorption of Gases and Vapors in Micropores, in: D.A. Cadenhead, J.F. Danielli, M.D. Rosenberg (Eds.), Prog. Surf. Membr. Sci., Academic Press: New York, New York, 1975: pp. 1–70. doi:10.1016/b978-0-12-571809-7.50006-1.

[50] W. Ruland, B. Smarsly, X-ray scattering of non-graphitic carbon: an improved method of evaluation, J. Appl. Crystallogr. 35 (2002) 624–633. doi:10.1107/S0021889802011007.

[51] A.K. Kercher, D.C. Nagle, Microstructural evolution during charcoal carbonization by X-ray diffraction analysis, Carbon N. Y. 41 (2003) 15–27. doi:10.1016/S0008-6223(02)00261-0.

[52] G.A. Zickler, B. Smarsly, N. Gierlinger, H. Peterlik, O. Paris, A reconsideration of the relationship between the crystallite size La of carbons determined by X-ray diffraction and Raman spectroscopy, Carbon N. Y. 44 (2006) 3239–3246. doi:10.1016/j.carbon.2006.06.029.

[53] M. Jagtoyen, F. Derbyshire, Activated carbons from yellow poplar and white oak by H3PO4 activation, Carbon N. Y. 36 (1998) 1085–1097. doi:10.1016/S0008-6223(98)00082-7.

[54] A. Kumar, H.M. Jena, Preparation and characterization of high surface area activated carbon from Fox nut (Euryale ferox) shell by chemical activation with H 3 PO 4, Results Phys. 6 (2016) 651–658. doi:10.1016/j.rinp.2016.09.012.

[55] F. Quesada-Plata, R. Ruiz-Rosas, E. Morallón, D. Cazorla-Amorós, Activated Carbons Prepared through H 3 PO 4 -Assisted Hydrothermal Carbonisation from Biomass Wastes: Porous Texture and Electrochemical Performance, Chempluschem. 81 (2016) 1349–1359. doi:10.1002/cplu.201600412.

[56] F. Yu, S. Li, W. Chen, T. Wu, C. Peng, Biomass- Derived Materials for Electrochemical Energy Storage and Conversion: Overview and Perspectives, ENERGY Environ. Mater. 2 (2019) 55–67. doi:10.1002/eem2.12030.

[57] J. Wang, P. Nie, B. Ding, S. Dong, X. Hao, H. Dou, et al., Biomass derived carbon for energy storage devices, J. Mater. Chem. A. 5 (2017) 2411–2428. doi:10.1039/C6TA08742F.

[58] D. Aurbach, B. Markovsky, G. Salitra, E. Markevich, Y. Talyossef, M. Koltypin, et al., Review on electrode-electrolyte solution interactions, related to cathode materials for Li-ion batteries, J. Power Sources. 165 (2007) 491–499. doi:10.1016/j.jpowsour.2006.10.025.

[59] P. Verma, P. Maire, P. Novák, A review of the features and analyses of the solid electrolyte interphase in Li-ion batteries, Electrochim. Acta. 55 (2010) 6332–6341. doi:10.1016/j.electacta.2010.05.072.

[60] M. Winter, J.O. Besenhard, M.E. Spahr, P. Novák, Insertion electrode materials for

rechargeable lithium batteries, Adv. Mater. 10 (1998) 725–763. doi:10.1002/(SICI)1521-4095(199807)10:10<725::AID-ADMA725>3.0.CO;2-Z.

[61] M.B. Pinson, M.Z. Bazant, Theory of SEI Formation in Rechargeable Batteries: Capacity Fade, Accelerated Aging and Lifetime Prediction, J. Electrochem. Soc. 160 (2013) A243–A350. doi:10.1149/2.044302jes.

[62] C.J. Wen, C. Ho, B. a. Boukamp, I.D. Raistrick, W. Weppner, R. a. Huggins, Use of electrochemical methods to determine chemical-diffusion coefficients in alloys: application to 'LiAI,' Int. Mater. Rev. 26 (2012) 253–268. doi:10.1179/095066081790149195.

[63] C. Ho, I.D. Raistrick, R.A. Huggins, Application of A-C Techniques to the Study of Lithium Diffusion in Tungsten Trioxide Thin Films, J. Electrochem. Soc. 127 (1980) 343–350. doi:10.1149/1.2129668.

[64] D. Aurbach, M.D. Levi, E. Levi, A review on the solid-state ionics of electrochemical intercalation processes: How to interpret properly their electrochemical response, Solid State Ionics. 179 (2008) 742–751. doi:10.1016/j.ssi.2007.12.070.

[65] B.A. Boukamp, A package for impedance/admittance data analysis, Solid State Ionics. 18–19 (1986) 136–140. doi:10.1016/0167-2738(86)90100-1.

[66] D. Di Lecce, R. Verrelli, D. Campanella, V. Marangon, J. Hassoun, A New CuO-Fe2O3-Mesocarbon Microbeads Conversion Anode in a High-Performance Lithium-Ion Battery with a Li1.35Ni0.48Fe0.1Mn1.72O4 Spinel Cathode, ChemSusChem. 10 (2017) 1607–1615. doi:10.1002/cssc.201601638.

[67] D. Aurbach, Review of selected electrode–solution interactions which determine the performance of Li and Li ion batteries, J. Power Sources. 89 (2000) 206–218. doi:10.1016/S0378-7753(00)00431-6.

[68] E. Buiel, J.R. Dahn, Li-insertion in hard carbon anode materials for Li-ion batteries,

Electrochim. Acta. 45 (1999) 121–130. doi:10.1016/S0013-4686(99)00198-X.

[69] S.L. Candelaria, Y. Shao, W. Zhou, X. Li, J. Xiao, J.G. Zhang, et al., Nanostructured carbon for energy storage and conversion, Nano Energy. 1 (2012) 195–220. doi:10.1016/j.nanoen.2011.11.006.

[70] J. Hassoun, K.S. Lee, Y.K. Sun, B. Scrosati, An advanced lithium ion battery based on high performance electrode materials, J. Am. Chem. Soc. 133 (2011) 3139–3143. doi:10.1021/ja110522x.

[71] G.A. Elia, J. Wang, D. Bresser, J. Li, B. Scrosati, S. Passerini, et al., A new, high energy Sn-C/Li[Li0.2Ni0.4/3Co 0.4/3Mn1.6/3]O2 lithium-ion battery, ACS Appl. Mater. Interfaces. 6 (2014) 12956–12961. doi:10.1021/am502884y.

[72] D. Di Lecce, S. Levchenko, F. Iacoviello, D.J.L. Brett, P.R. Shearing, J. Hassoun, X- ray Nano- computed Tomography of Electrochemical Conversion in Lithium- ion Battery, ChemSusChem. (2019) cssc.201901123. doi:10.1002/cssc.201901123.

[73] D. Molina Piper, S.-B. Son, J.J. Travis, Y. Lee, S.S. Han, S.C. Kim, et al., Mitigating irreversible capacity losses from carbon agents via surface modification, J. Power Sources. 275 (2015) 605–611. doi:10.1016/j.jpowsour.2014.11.032.

[74] A. Eftekhari, LiFePO 4 /C nanocomposites for lithium-ion batteries, J. Power Sources. 343 (2017) 395–411. doi:10.1016/j.jpowsour.2017.01.080.

[75] J. Vetter, P. Nov??k, M.R. Wagner, C. Veit, K.C. M??ller, J.O. Besenhard, et al., Ageing mechanisms in lithium-ion batteries, J. Power Sources. 147 (2005) 269–281. doi:10.1016/j.jpowsour.2005.01.006.